Monazite U–Th–Pb EPMA and zircon U–Pb SIMS chronological constraints on the tectonic, metamorphic, and thermal events in the inner part of the Variscan orogen, example from the Sioule series, French Massif Central

Damien Do Couto, Michel Faure, Romain Augier, Alain Cocherie, Philippe Rossi, Xian-Hua Li, Wei Lin

Monazite U-Th-Pb EPMA and zircon U-Pb SIMS chronological constraints on the tectonic, metamorphic and thermal events in the inner part of the Variscan orogen, example from the Sioule series, French Massif Central

Damien Do Couto[1,2], Michel Faure[1*], Romain Augier[1], Alain Cocherie [3], Philippe Rossi[3]
Xian-Hua Li[4], Wei Lin[4]

1: Université d'Orléans-CNRS/INSU, Institut des Sciences de la Terre d'Orléans (ISTO), Campus Géosciences, 1A Rue de la Férollerie 45071 Orléans Cedex 2, France
(*corresponding author: michel.faure@univ-orleans.fr)
2: Département des Sciences de la terre, 13 rue des Maraîchers, 1205 Genève, Switzerland
3: BRGM, Av. Claude-Guillemin, BP 36009, 45060 Orléans Cedex 2 France
4: State Key Laboratory of Lithospheric Evolution, Institute of Geology and Geophysics, Chinese Academy of Sciences, Beijing 100029, China

Abstract

In the northern Variscan French Massif Central, the Sioule metamorphic series exposes from top to bottom the tectonic superposition of the Upper Gneiss Unit (UGU), Lower Gneiss Unit (LGU), and Para-autochthonous Unit (PAU). The nappe stacking developed throughout two prograde syn-metamorphic events: D_1 is a top-to-the SW shearing coeval with a probable Devonian migmatization, and D_2 is a top-to-the NW shearing event. Both events were completed before the unconformable deposition of the undeformed and unmetamorphozed "Tufs anthracifères" formation, dated at ca 330 Ma (Late Visean). Furthermore, the UGU experienced a high pressure metamorphism ascribed to a D_0 event during which eclogite or granulite crystallized in several parts of the UGU. Monazite U-Th-Pb, and zircon U-Pb SIMS

datings were carried out in order to constrain the ages of these D_0, D_1, and D_2 tectonic-metamorphic events. These new geochronological results are placed in a P-T-t diagram constructed for the UGU, LGU, and PAU. Monazite sampled in UGU, LGU, PAU rocks yields similar 365-350 Ma ages consistent with the D_2 event dated in other places of the French Massif Central. A zoned monazite grain from a granulitic paragneiss yields 416±15 Ma and 362±14 Ma ages interpreted as those of the D_0 and D_2 events, respectively. Zircon from the same granulitic paragneiss yields SIMS ages at 343±2 Ma, and 328±2 Ma that are interpreted as recrystallization processes associated with post-thickening thermal events, possibly recording the onset of orogenic collapse of the Northern Massif Central. It is worth to note that neither monazite nor zircon recorded the D_1 event.

Key words Variscan orogeny, monazite chemistry, monazite U-Th-Pb chemical dating, zircon SIMS geochronology, granulite facies, monazite chemistry, French Massif Central

Introduction

Dating the syn-metamorphic rocks and their related ductile fabrics remains a challenge. Indeed, many of the common metamorphic phases such as biotite, muscovite, feldspar, and amphibole can be dated by the $^{40}Ar/^{39}Ar$ method, however it is well acknowledged that this chronometer is highly sensitive to any late thermal perturbation, thus the radiometric ages obtained by this method may represent cooling ages or "re-opening" ages rather than genuine crystallization age of the dated minerals (see Jourdan et al 2014 for a recent review). Zircon is also a common accessory phase used for U-Pb geochronology. Due to analytical improvements, punctual measurements using SIMS, SHRIMP or LA-ICP-MS technique, zircon yields precise age, however as for the $^{40}Ar/^{39}Ar$ method, the significance of zircon U-Pb geochronology must be carefully considered for dating metamorphic rocks since zircon may crystallize or recrystallize at various stages of the rock history, including initial magmatism formation stage for igneous protoliths. Monazite that may crystallize either from magma or during metamorphic reactions appears as one of the most useful phase to assess the timing of tectono-metamorphic events. Although separated monazite grains can be dated by SIMS or LA-ICP-MS, the *in-situ* approach that preserves the textural relationships between minerals allows the deciphering of superimposed magmatic and/or metamorphic high-temperature stages. Furthermore, the size of the analytical spot (*ca* 20 µm) for LA-ICP MS measurements generally prevents this detailed investigation as metamorphic monazite is often small-sized, chemically zoned or partly dissolved. Nevertheless, though involving a non-isotopic technique, with a *ca* 5 to15 Ma uncertainty, larger than the isotopic methods, the monazite U-Th-Pb EPMA method can provide one of the best estimate of the metamorphic mineral crystallization ages in polymetamorphic terranes.

Due to the abundance of metapelitic and felsic magmatic protoliths, the Variscan belt appears as a good example to determine the ages of successive tectono-metamorphic events,

in polymetamorphosed and polydeformed domains, particularly when thermo-barometric conditions preclude the use of temperature-sensitive geochronological methods such as $^{40}Ar/^{39}Ar$. This paper aims to apply the monazite U-Th-Pb EPMA chemical, and zircon U-Pb SIMS dating methods to the Sioule metamorphic series, in the Northern part of the Variscan French Massif Central since in this area, the tectonic-metamorphic succession is already well established, but radiometric constraints still rare, as presented in the following sections (e.g. Faure et al. 1993, 2002; Schulz et al. 2001; Schulz 2009).

Geological outline of the Variscan French Massif Central

The stack of nappes

The French Massif Central (FMC thereafter) is an important segment of the Variscan Belt that results of a complex interplay between two main continents, namely Gondwana, and Laurussia, and several intervening microcontinents such as Avalonia, Mid-German Crystalline Rise, and Armorica (e.g. Matte 2001; Cocks 2000; Faure et al. 2005; Murphy et al. 2011). It is now well acknowledged that the bulk architecture of the French Massif Central, alike the southern part of the Massif Armoricain or the Vosges-Black Forest massif, is a stack of metamorphic nappes developed diachronously from Late Silurian to Early Carboniferous at the expense of the north Gondwana margin (Matte 1986; Ledru et al. 1989; Faure et al. 2005, 2009; Lardeaux et al. 2014; Fig . 1).

From bottom to top, and South to North, the following units are recognized (Figs. 1, 2). *1) The foreland basin* develops in the southernmost part of the Massif Central. It is an Early Carboniferous (Visean-Serpukhovian) turbiditic basin that extends southward below the coastal plain of the Mediterranean Sea. *2) The Paleozoic Fold-and-Thrust Belt* consists of Early Cambrian to Visean unmetamorphosed sedimentary rocks displaced to the South as

thrust sheets or kilometre-scale recumbent folds well. There, the Early Devonian (i. e. Lochkovian, 416-411 Ma) unconformity argues for an Early Paleozoic tectonic event (at ca 420-400 Ma), which is also recorded to the North of the Massif Central in the Lower and Upper Gneiss metamorphic units (cf. below). *3) The Para-autochthonous Unit* that overthrusts the Paleozoic Fold-and-Thrust Belt is formed by greenschist to epidote-amphibolite facies metapelites, metagreywackes, quartzites, and a small amount of marbles and metabasites. In the northern Massif Central, the Para-autochthonous Unit crops out in tectonic windows surrounded by the Lower Gneiss Unit. In the Cévennes area, some granitic plutons, now transformed into orthogneiss, intruding the series, yield Cambrian to Early Ordovician zircons (Bé Mézème et al. 2006). *4) The Lower Gneiss Unit (LGU)* is composed of metagreywackes, metapelites, and metarhyolites intruded by Cambrian to Early Ordovician porphyritic alkaline granitoids transformed into augen orthogneiss during the tectonic-metamorphic events. The LGU underwent a Middle Devonian metamorphism leading to crustal melting coeval with a ductile shearing dated in the Limousin at 375-370 Ma (Faure et al. 2008) and attributed to the D_1 event (cf below). Moreover, the LGU also experienced a medium pressure/medium temperature metamorphism characterized by a biotite-garnet-staurolite assemblage, dated at ca. 360-350 Ma (Costa 1989; Melleton et al. 2009), and attributed to the D_2 event. *5) The Upper Gneiss Unit (UGU)* forms the overlying nappe whose the main protoliths are metapelites and metagrauwackes. This unit contains high-pressure rocks, such as eclogites or high pressure (HP) granulitic orthogneiss that may locally reach the coesite-eclogite facies (Santallier 1981; Pin and Vielzeuf 1988; Lardeaux et al. 2001; Berger et al., 2010). The upper part of the UGU consists of Devonian migmatites, yielding zircon U-Pb ages at *ca* 385-380 Ma, attributed to the D_1 event, and formed by the partial melting of pelitic and quartzo-feldspathic rocks (Duthou et al. 1994; Faure et al. 2008). These rocks contain amphibolite blocks derived from retrogressed eclogites that did not experience partial

melting. The HP metamorphism is dated at ca 420-400 Ma by U-Pb and Sm-Nd methods in several locations (Pin and Peucat 1986; Paquette et al. 1995; Faure et al. 2005).

The five units described above represent the classical nappe pile of the FMC in which the metamorphism increases from bottom to top. Furthermore, in the northern part of the French Massif Central, the undeformed and unmetamorphozed "Tuffs anthracifères" series, which consists of terrigenous rocks (sandstone, shales, conglomerates), coal measures, and felsic magmatic rocks (dacites and rhyolites), is dated as Late Visean (*ca* 330 Ma, Bruguier et al. 1998). These rocks unconformably cover Late Devonian-Early Carboniferous plutonic or metamorphic rocks of the UGU and LGU. The "Tuffs anthracifères" series provides a major time constraint for the evolution of the French Massif Central. As the "Tuffs anthracifères" series is coeval with the development of the Fold-and-Thrust Belt, it supports the north-south diachronism in the deformation at the scale of the entire massif.

The polyphase tectono-metamorphic evolution

The Variscan geodynamic evolution of the French Massif Central remains disputed. Some authors (e.g. Matte 1986; Ledru et al. 1989) consider that the formation of the FMC results of a continuous north-directed oceanic then continental subduction from early Silurian to early Carboniferous. In contrast, other authors (e.g. Pin 1990; Faure et al. 1997, 2008, 2009) argue for a polycyclic evolution. The Early Silurian to Early Devonian events correspond to the Eo-Variscan cycle due the collision of the Armorica microcontinent with the north Gondwana margin. From Middle Devonian to Early Carboniferous, the Variscan belt develops due to the southward subduction of the Rheic Ocean below Gondwana followed by the collision of Gondwana with Laurussia. In spite of differences between the two geodynamic scenarii, most of authors agree on the main tectonic, metamorphic, and magmatic events. Six tectono-metamorphic events are recognized (Faure et al. 2009).

141 The earliest event, D_0, corresponds to the high to ultra high-pressure metamorphism
142 recorded in the eclogite facies rocks of the UGU. Most of the HP rocks derive from mafic
143 protoliths, but also HP relics are also found in orthogneiss are locally found. In the Lyonnais
144 area, the UGU eclogites record pressure and temperature conditions of 1.8-2 GPa and 650-
145 750°C, respectively (Lardeaux et al. 2001). On the basis of the HP metamorphism, the D_0
146 event took place around 415 Ma (Pin and Peucat 1986).

147 The Early to Middle Devonian, tectonic-metamorphic event D_1, is coeval with the
148 crustal melting of the metapelites and orthogneiss of the UGU and LGU, whereas mafic rocks
149 are preserved as amphibolite restitic blocks in migmatites. The migmatisation is dated as
150 Middle Devonian (385-375 Ma) in the Limousin or Lyonnais areas (Duthou et al. 1994, Faure
151 et al. 2008 and enclosed references). P-T estimates from garnet-plagioclase and garnet-biotite
152 pairs in migmatites, indicate metamorphic conditions of 0.7±0.05 GPa and 700±50°C
153 respectively (Mercier et al. 1991; Roig and Faure 2000). The flat-lying foliation exhibits a
154 NE-SW striking (N30 to N60E) stretching lineation marked by fibrolitic sillimanite or biotite
155 in migmatites, and biotite or amphibole in amphibolites. Shear criteria indicate a top-to-the-
156 SW displacement (Ledru et al.1989; Faure et al. 1997; Roig and Faure 2000). Amphibolite in
157 the northern Massif Central yields biotite and hornblende $^{40}Ar/^{39}Ar$ cooling ages ranging from
158 390 Ma to 381Ma (Costa and Maluski 1988; Boutin and Montigny 1993). In northeastern
159 Massif Central, or Morvan area, Middle Devonian unmetamorphosed and undeformed
160 sedimentary rocks unconformably overlying migmatites with eclogite relics suggest that, at
161 least in the northern part of the Massif Central, the HP rocks were already exhumed before the
162 Middle Devonian (Faure et al. 1997).

163 In the LGU, UGU, the dominant fabric is a NW-SE trending stretching lineation
164 developed either on flat-lying or steeply dipping foliations, which is attributed to the D_2 event
165 (Faure et al. 2005, 2008). Thermo-barometric constraints are well established in the Limousin

166 and Rouergue areas (Duguet et al. 2006; Bellot and Roig 2007). In the UGU, the syn-D_2
167 minerals, crystallized along the NW-SE lineation, indicate 0.7-1 GPa and 600-700°C
168 metamorphic conditions. Paragneiss belonging to the LGU yield nearly similar conditions of
169 0.8-1 GPa and 550-600°C. In the LGU, amphibolites that never experienced the high-pressure
170 event indicate 0.8-1 GPa and 700-800°C metamorphic conditions (Santallier 1981). The D_2,
171 event, characterised by a top-to-the-NW ductile shearing, is widely documented from the
172 southeast Massif Central up to the Southern part of the Massif Armoricain. This deformation
173 is stratigraphically dated as pre-Early Visean (i.e. older than 345 Ma) by the unconformity
174 recognized in the Brévenne area (e.g. Leloix et al., 1999 and enclosed references, Fig. 1). The
175 age of the syn-D_2 MP/MT metamorphism is constrained by $^{40}Ar/^{39}Ar$ method on biotite,
176 muscovite and amphibole, and by EPMA on monazite between 360 and 350 Ma (Costa 1989;
177 Leloix et al. 1999; Melleton et al. 2009).

178 The syn-metamorphic D_3 deformation is recognized only in the Para-autochthonous
179 Unit of the southern part of the Massif Central that experienced a first deformation at *ca* 340-
180 335 Ma (Caron 1994; Faure et al. 2005). Further south, south-verging recumbent folds and
181 thrusts of the Paleozoic series dated of Late Visean-Early Namurian (*ca* 325 Ma) by the syn-
182 orogenic sediments of the foreland basin, are also related to the D_3 event. This progressive
183 southward younging of the nappe tectonics is coeval with the development of a flat-lying
184 foliation and a N-S to NE-SW striking stretching lineation. In contrast to the southern part of
185 the Massif Central, in its northern part, the Late Visean deformation develops under brittle
186 conditions. It is represented by a NW-SE stretching, related to the emplacement of NE-SW
187 striking dykes of basalt, dacite, and microgranite in the Tuff Anthracifères series. This
188 deformation is interpreted as the onset of the syn-orogenic extension (Faure 1995).

189 Ductile normal faults, such as Argentat or Nantiat faults, coeval with Serpukhovian-
190 Bashkirian (or Namurian-Westphalian in W. European stratigraphy, *i.e.* 325-315 Ma)

synkinematic granite emplacement, argue for an extensional tectonic phase named the D_4 event (Faure 1995). As shown by petrofabric and AMS studies, most of the Late Carboniferous leucogranite and porphyritic monzogranite plutons and their metamorphic aureoles exhibit a well-defined NW-SE trending mineral or stretching lineation (Talbot et al. 2005; Joly et al. 2007). The tectonic-plutonic D_4 event, widespread in the entire Massif Central, is interpreted as a syn-orogenic extensional process since at this time, compression was still active in the northern and southern outer zones of the Variscan belt, such as Ardenne and Montagne Noire-Pyrénées, respectively.

The last phase in the structural evolution of the French Massif Central is a Late Carboniferous (Kasimovian-Ghzelian, or Stephanian) D_5 late-orogenic extensional event that is distinguished from the previous one by the NNE-SSW strike of the maximum stretching direction. Intramontane coal basins develop either as half-grabens or left-lateral pull-aparts depending on the strike and kinematics of the bounding fault that controls the basin opening and sedimentary infill.

The Sioule metamorphic series

The bulk architecture

Located in the northern part of the French Massif Central, the Sioule metamorphic series is bound to the west by the Late Carboniferous Sillon Houiller sinistral wrench fault, and to the east by the Oligocene Ebreuil and Limagne grabens (Figs. 1, 2). The Trében Massif and the S^{te}-Christine wrench fault are the northern and southern limits of the Sioule metamorphic series, respectively (Fig. 2). The metamorphic series is intruded by two granitic plutons. The Pouzol-Servant porphyritic microgranite is a biotite granite dated at *ca* 330 Ma (Pin, 1991). The Echassières leucogranite is a small, differentiated, peraluminous pluton dated at *ca* 310 Ma (Duthou and Pin 1987; Cheilletz et al. 1992). The Sioule series is a classic example of an inverted metamorphic sequence in the Massif Central (Grolier 1971). Three lithological and

structural units have been described (Richard 1938; Grolier 1971; Faure et al. 1993). From top to bottom, they are: a) an upper unit composed of biotite-sillimanite gneiss, and biotite-sillimanite± cordierite migmatite developed at the expense of the underlying gneiss that enclose a few meter-sized boudins of kyanite-garnet-plagioclase high-pressure granulitic paragneiss partly retrogressed under amphibolite facies conditions (Ravier and Chenevoy 1979). This unit is correlated with the Upper Gneiss Unit (UGU) of the French Massif Central (cf section 2); b) an intermediate unit formed by biotite-muscovite-sillimanite-K feldspar-garnet paragneiss corresponding to the Lower Gneiss Unit (LGU), and c) a biotite-staurolite-garnet micaschist that crops out around the Echassières pluton. This unit, which is structurally below the two micas paragneiss of the LGU, lacks of orthogneiss and anatectic melts, it is therefore correlated with the Para-autochthonous Unit (PAU).

Structural outline of the Sioule metamorphic series

In the study area, the observed structures, and the related kinematics account well for a multistage tectonic evolution. In agreement with previous works (Grolier 1971; Feybesse and Teygey 1987; Faure et al. 1993; Schulz et al. 2001; Schulz 2009), the foliation is folded by NNW-SSE trending km-scale upright synform and antiform (Fig.2). A WNW-ESE striking stretching and mineral lineation is well developed in the foliation plane of the PAU, LGU, and UGU. Microscope-scale shear criteria, such as sigmoidal micas, asymmetric pressure shadows around feldspar or garnet, and S-shaped inclusion trails in garnet consistently indicate a top-to-the WNW shearing (Faure et al. 1993; Schulz 2009). These microstructural features are relevant to the D_2 event of the Massif Central.

In the UGU, in addition to the main NW-SE D_2 deformation, a NNE-SSW striking mineral and stretching lineation is also recognized (Grolier 1971; Feybesse and Teygey 1987; Faure et al. 1993). This deformation, characterized by elongated biotite-sillimanite

aggregates, stretched K-feldspar, and axes of intrafolial folds parallel to the stretching lineation, is associated with top-to-the SSW kinematic indicators. A Barrovian-type metamorphism with biotite-sillimanite-K-feldspar assemblage is coeval with this deformation event that appears less developed, and older, than the NW-SE D_2 one. In the upper part of the UGU, the biotite-sillimanite±cordierite migmatite exhibits also the NNE-SSW mineral and stretching lineation, with similar top-to-the-SW kinematics as those observed in the underlying biotite-sillimanite gneiss. By correlation with the general tectonic-metamorphic pattern of the FMC, this early phase is correlated with the D_1 event, thus a Middle Devonian age, dated from 385 to 375 Ma is suggested (Faure et al. 2009) but not documented yet.

Furthermore, top-to-the-WNW and top-to-the-ESE shearing, characterized by shear bands cutting through the regional foliation, sericite pressure shadows upon cataclazed staurolite or garnet porphyroclasts, develop around the Echassières pluton. These kinematic indicators, coeval with greenschist facies metamorphic conditions, are related to the emplacement of the Echassière leucogranite pluton in an extensional setting. Thus this deformation phase corresponds to the D_4 event (Faure et al. 2009).

In contrast with other areas of the French Massif Central, mafic eclogites formed during the earliest D_0 event are not recognized in the Sioule area. Nevertheless, kyanite-garnet-plagioclase-rutile high-pressure granulitic gneiss, garnet-pyroxenite, and rare serpentinite boudins are mapped in the UGU (Grolier 1971; Ravier and Chenevoy 1979). These rocks argue for an early HP event probably equivalent to the D_0 one. Moreover, in paragneiss, as shown by the symplectitic texture, these HP garnet and kyanite grains are surrounded by a biotite-sillimanite or muscovite assemblage representative of an amphibolite facies retrogression developed during the D_1 or D_2 events (Fig. 3). As in most areas of the Massif Central, the planar and linear fabrics related to the D_0 event have been erased by subsequent metamorphic recrystallization or deformation events. But since syn-D_0 minerals,

such as kyanite, core of garnet, and possibly monazite are preserved, the rocks may still be suitable to yield the age of the HP event.

Available time constraints in the Sioule metamorphic series are currently limited (Faure et al., 2002; Schulz, 2009). The Late Visean Pouzol-Servant microgranite and the Bashkirian-Moscovian Echassières leucogranite intrude the already metamorphosed and ductilely deformed series, and thus provide the upper time limit for the D_0, D_1, and D_2 tectono-metamorphic events. An $^{40}Ar/^{39}Ar$ survey has been carried out in the metamorphic units of the Sioule series (Faure et al. 2002). All the minerals, whatever the rock type or the tectonic unit, yielded similar ca 335-330 Ma ages that were interpreted as the Late Visean thermal overprint since these ages are similar, within the errors, to the age of the "Tuffs Anthracifères" event. Thus, the ages of the different pre-Late Visean tectono-metamorphic events in the Sioule series remain presently unknown.

Sampling and petrological description

Twenty-four samples representative of the different metamorphic assemblages cropping out in the Sioule series have been petrologically studied in order to bring the time constraints on the metamorphic evolution of this series. After detailed microscopic observations, five samples were selected due to their suitable parageneses and textures to ensure the presence of accessory minerals such as monazite and zircon developed during the D_1 and D_2 tectono-metamorphic events. The sample location in the Sioule nappe pile, and the GPS position, are provided in Figure 2 and Table 1, respectively. The PAU is represented by a staurolite-garnet micaschist (SO3) located to the East of the Echassières pluton. The LGU is represented by a two-mica paragneiss (SO17) to the SE of the same pluton. The UGU is represented by a biotite-sillimanite gneiss (SO7), a migmatitic gneiss (SO11), and a biotite-kyanite-garnet paragneiss (SO15), located on both limbs of the antiform. The microstructural descriptions

herein refer to thin sections cut parallel to the stretching lineation (X) and perpendicular to the foliation plane (Z), i.e. in the XZ plane of the finite strain ellipsoid.

Sample SO3, belonging to the Para-autochthonous unit, consists of quartz, feldspar, biotite, muscovite, garnet, staurolite, sericite, and chlorite. In the field, structural observations show a low-angle ESE plunging foliation, and a N105E to N115E striking mineral lineation (Fig. 3a2). The foliation cut by shear bands, and sigmoidal quartz veins indicate a top-to-the-SE sense of shear (Fig. 3a1). Under the microscope, cataclazed garnet and staurolite surrounded by an asymmetric mantle of sericite developed during retrogression of the main assemblage indicate the same sense of shear (Fig 4a). Furthermore, garnet exhibits sigmoidal inclusions of quartz and opaque minerals indicating an earlier foliation. The asymmetry of these inclusions indicates a synkinematic crystallisation of these porphyroblasts during a noncoaxial deformation that is not in agreement with the top-to-the-SE sense of shear, but instead argues for a top-to-WNW sense of shear developed during the D_2 event. According to Schulz et al (2001), the thermobarometry from the PAU micaschist indicates a prograde P-T evolution with increasing temperatures from 450°C to 600°C under slightly increasing pressure from 0.7 to 0.8 GPa, followed by a P and T decrease indicated by the formation of retrogressive sericite during the decompression. Scan Electron Microscope (SEM) backscattered electron (BSE) observation of sample SO3 reveals the presence of 50 to 100 µm sized, homogeneous, monazite grains included into biotite or crystallized along grain boundaries.

Sample SO17 is a two-mica paragneiss presenting traces of incipient migmatization belonging to the LGU with a segregation of thick quartz-feldspar and thin biotite and sillimanite layers. The flat lying foliation contains a NW-SE striking mineral and stretching lineation related to the D_2 event. The mineral assemblage consists of quartz, feldspar, biotite, muscovite, chlorite, and accessory minerals including sillimanite, Fe-Ti-oxides, and monazite.

317 Muscovite often presents a clear secondary character, growing without preferred orientation
318 while biotite is partially altered into chlorite in line with a late thermal overprint (Faure et al.
319 2002). Biotite contains large subeuhedral monazite grains of *ca* 80-120 µm size. Monazite
320 also occurs as *ca* 80-100µm euhedral inclusions in biotite or quartz. Despite the existence of
321 these two occurrences, in SEM BSE imaging, the monazite grains exhibit homogeneous
322 internal textures without zoning.

323 *Sample SO7* is a biotite-sillimanite migmatitic paragneiss belonging to the UGU
324 collected near Moulin du Bouchet (Fig. 2). This rock is composed of quartz, feldspar, garnet,
325 biotite, muscovite, rare staurolite and fibrolitic sillimanite. Field observations of coarse-
326 grained quartz-feldspar leucosome parallel to the foliation indicate that this rock underwent a
327 limited partial melting. The biotite-sillimanite assemblage defines a pervasive foliation and a
328 N50E striking mineral and stretching lineation that can be assigned to the regional D_1
329 deformation. However, as already pointed out by Schulz (2009), the subeuhedral shape of the
330 garnet argues for a static growth after the development of the D1 structures. According to
331 Schulz et al. (2001), the biotite-sillimanite gneiss of Moulin de Bouchet, which is located
332 close to our sample SO7, underwent a prograde metamorphic evolution at low pressure (0.4-
333 0.6 GPa) and high temperature (650°C-700°C). Thus, this biotite-sillimanite paragneiss might
334 have also experienced the D_2 event, although typical D_2 NW-SE stretching lineation is not
335 observed. In this rock, all the analyzed monazite grains, observed in SEM BSE mode, are
336 homogeneous inclusions in biotite (Fig. 4b).

337 *Sample SO11*, collected at Pont de Menat (Fig. 2) is a migmatitic paragneiss belonging
338 to the upper part of the UGU. This rock is composed of alternations of coarse-grained quartz-
339 feldspar leucosome and fine-grained biotite-fibrolitic sillimanite-garnet melanosome. Field
340 observation shows the occurrence of a pervasive deformation characterized by a flat-lying
341 foliation and a N120E trending mineral and stretching lineation assigned to the D_2 event (Fig.

342 3 c). All the analyzed monazite grains observed in SEM BSE mode are homogeneous
343 inclusions in biotite (Fig. 4c).
344 *Sample SO15* is a kyanite-garnet ± rutile paragneiss coming from Saugères (Fig. 2).
345 This rock is composed of biotite, feldspar, quartz, garnet, and kyanite. Garnet and kyanite are
346 1-5 mm sized clasts included in a well-foliated granoblastic matrix composed of quartz,
347 feldspar, and small biotite flakes (Fig. 3d). The kyanite-garnet assemblage that formed in
348 high-pressure granulite facies underwent an amphibolite facies retrogression as shown by
349 biotite overgrowths around garnet porphyroclasts (Ravier and Chenevoy 1979; Fig. 4d).
350 Monazite inclusions in garnet and in biotite exhibit a core-rim chemical zoning.
351
352 **Monazite EPMA chemical dating**
353 Analytical method and strategy
354 Due to its high U and Th contents, and negligible initial Pb content (Parrish 1990), it is
355 now well acknowledged that a crystallization (or recrystallization) age can be determined
356 from monazite on the basis of its chemical composition in U, Th, and Pb determined by
357 electron probe microanalysis (EPMA). Such a simple and fast technique has been successfully
358 applied to several plutonic or metamorphic rocks (e.g. Suzuki and Adachi, 1991; Montel et
359 al., 1996; Cocherie et al., 1998, 2005; Cocherie and Albarède, 2001; Schulz et al., 2009; Faure
360 et al., 2010, and enclosed references). Monazite is a common accessory mineral in
361 metamorphic rocks, especially in metapelites. It crystallizes in a wide range of P-T conditions,
362 from greenschist facies (Cabella et al. 2001; Rasmussen et al. 2001) to amphibolite (Smith
363 and Barreiro 1990; Kohn and Malloy 2004) and granulite facies (Bé Mézème et al. 2006; Mc
364 Farlane and Frost 2009) in rocks metamorphosed under Barrovian P-T gradient during
365 prograde or retrograde paths. Previous studies have shown also that monazite can crystallize
366 in blueschist (Janots et al. 2006) or even eclogite facies (Nagy et al. 2002). Consequently,

analyzed monazite grains must be linked with petrological studies to delimit their P-T crystallization domain. The chemical composition of monazite is an important parameter in order to discuss the radiometric ages.

In situ chemical U-Th-Pb dating of monazite has been developed over the past fifteen years allowed by technological progress performed on electron microprobe analyses (EPMA; Suzuki and Adachi 1991; Montel et al. 1996; Cocherie et al. 1998, 2005). The method uses the radiochronometer between U and Th parent and Pb radiogenic elements, considering the restricted lead diffusion in monazite lattice below 900°C (Cocherie et al. 1998). The determination of U, Th and Pb contents can be performed directly by EPMA *in situ* analyses on polished thin section after textural optical microscope observation of crystallisation-deformation relationships between the constitutive minerals, and monazite internal structure determination using a SEM in BSE mode. This approach provides petrological constraints on the analyzed grains and thus allows us to discuss the significance of the calculated ages in the crystallisation-deformation history of the rock.

SEM BSE was used to define heterogeneous chemical compositional domains of monazite. In metamorphic rocks, contrasted chemical domains can be explained by the superimposition of metamorphic events that record a polyphase evolution during orogenic processes. Theoretical procedure to reduce the data and to calculate the average age from individual spot analyses is given by Cocherie and Albarède (2001), Cocherie et al. (2005), and Cocherie and Legendre (2007). The analysis of monazite grains directly from polished thin sections was performed by a Cameca SX 50 EPMA co-operated by BRGM-CNRS-Orléans University. An accelerating voltage of 20 kV, and a beam current of 100 nA were chosen as operating conditions. Synthetic phosphates, glasses and natural minerals were used as standards. The counting times (2/3 on peak and 1/3 on background) varies from 20s for Si, P, Ca, Nd, Gd, Y, Th, Ce and La, to 100s for U and 120s for Pb. Considering such parameters,

392 the detection limit for Th, U and Pb is 150 ppm (Cocherie and Albarede, 2001). X-ray
393 element maps were also recorded with an accelerating voltage of 20 kV and beam current of
394 100 nA, using the wavelength-dispersive spectrometers. Details on the analytical procedure
395 are the same as those used in Cocherie et al. (2005) and Faure et al. (2008, 2010). Age
396 calculations were done using the Isoplot/Ex (2.49) program of Ludwig (2001) and a Microsoft
397 Excel add-in program for determining U-Th-Pb ages from EPMA measurements (Pommier et
398 al. 2002). The 2σ errors given on individual ages depend on U, Th, and Pb contents, and are
399 calculated by propagating the uncertainties of these elements (at 95% confidence level).
400 Because the mean age of an homogeneous age population is directly drived from the isochron
401 plot Th/Pb vs U/Pb, only the uncertainty on these two parameters (Th/Pb and U/Pb) are
402 required to calculate the uncertainty on the mean age.
403 The strategy followed for this study was to derive time constraints for the monazite
404 included into the foliation forming biotite or in contact with it, in order to settle the
405 crystallisation time of the main foliation. Consequently, we concentrated on subeuhedral to
406 euhedral monazite grains. We focused on the dating of well-defined chemical domains so as
407 not to shuffle different heterogeneous domains that would yield different crystallization
408 periods.
409
410 Results
411 *Chemical composition of monazite grains.* SEM BSE images reveal chemically
412 homogeneous monazite grains for the four samples SO3, SO7, SO11, and SO17. Conversely,
413 the SO15 kyanite-garnet granulitic paragneiss sample presents zoned monazite grains. This
414 zonation corresponds to a core/rim zonation as described by Bé Mézème et al. (2006), mostly
415 due to the spatial distribution of U, Th and Pb. The EPMA analysis allows us to quantitatively
416 characterize the chemical composition of the dated grains. The average U/Pb and Th/Pb ratio

values, details concerning the number of spot analyses, and analyzed grains are provided in Table 1. Representative monazite chemical compositions with uncertainties for samples SO3, SO7, SO11, SO15, and SO17 are given in Table 2. For the granulitic gneiss (sample SO15), core and rim chemical data have been separated. Monazite chemical data for each samples are plotted in the Monazite ($2REEPO_4$) - Cheralite ($CaTh(PO_4)_2$) - Huttonite ($2ThSiO_4$) diagram (Linthout 2007; Fig. 5a), in order to show the relative substitution between end-member monazite phase and the cheralite or huttonite components (Fig. 5a). The cheralite substitution is always low, as already observed for various metamorphic environments (e.g. Franz et al. 1996; Cabella et al. 2001), and huttonite substitution is absent or negligible. In samples SO3, SO7, SO11 and SO17, monazite grains appear as homogeneous domains in BSE images, and the analytical data scatter along the cheralite-monazite axis showing clearly a common substitution. In sample SO15, the analyzed monazite grain is composed of two domains in the BSE images, with a light (i.e. dense) core and a dark (i.e. light) rim. Data plotted in the Monazite ($2REEPO_4$) - Cheralite ($CaTh(PO_4)_2$) - Huttonite ($2ThSiO_4$) diagram (Fig. 5a) show a relatively high Ce-monazite component into the core of the grain (white diamond) and a cheralite enriched rim (black diamond), corresponding to two different chemical domains. The (Th+U+Si+Pb) = f(REE+P) plot, modified from Franz et al. (1996), confirms the spread of the analytical data for samples SO3, SO7, and SO11 along the $CaThREE_{-2}$ axis corresponding to the cheralite substitution (Fig. 5b). Monazite chemical data from the staurolite micaschist SO3 (Fig. 5b) indicate a limited huttonite substitution pointed out by small vertical variation in Th+U+Si+Pb. Chemical data of monazite from biotite-sillimanite gneiss SO7 and SO11 show a more significant huttonite substitution than for SO3. The core and the rim of dated monazite grain from sample SO15 are characterized by two distinct sets of chemical compositions. The rim is richer in cheralite component than the core, even if huttonite substitution in each domain seems to be similar (Fig. 5b). X-ray maps depicting the

semiquantitative distribution of Th, Ca, and U confirm the chemical differences between the core and the rim of SO15 grain (Fig. 5d). These maps show that the monazite rim of monazite is enriched in Th and Ca compared to the core. The U content is relatively equivalent in the core and rim, except for an enriched fringe in the rim. This domain was not analyzed because of holes on the polished surface. Despite the presence of several small-sized domains indicated by the Ca and Th contents, the entire core is homogeneous in Th and U composition.

U-Th-Pb chemical dating. In this section, the ages of the analyzed monazite grains from samples SO3, SO 17, SO7, SO11, SO15 are presented following the tectonic order from bottom to top (Fig. 2).

Staurolite micaschist SO3. Data points are highly scattered on the Th/Pb vs. U/Pb diagram, leading to a small error envelope. The intercept ages are similar within errors, since the U-Pb age (intercept with U/Pb axis), and the Th-Pb age (intercept with Th/Pb axis) are at 379 +54/-62 Ma, and 357+26/-23 Ma, respectively. The calculated MSWD of 1.3 indicates that the population of 73 analyses is statistically homogeneous within the analytical errors (Wendt and Carl 1991). As a consequence, it is possible to calculate the mean age at the centroid where the precision is the best within the error envelope. Thus, the monazite grains yield a mean age of 363 ± 8 Ma (at 2σ confidence level; Fig. 6a).

Two-mica gneiss (SO17). Data points are weakly scattered on the Th/Pb vs. U/Pb diagram, leading to a large error envelope. The intercept ages are similar within errors, since the intercept U-Pb age and the intercept Th-Pb age are at 399 +44/-53 Ma, and 328+31/-26 Ma, respectively. The calculated MSWD of 0.63 indicates that the population of 38 analyses is statistically homogeneous within the analytical errors (Wendt and Carl 1991). As a consequence, it is possible to calculate the mean age at the centroid where the precision is the

467 best within the error envelope. Thus, the monazite grains yield a mean age of 351 ± 5 Ma (at
468 2σ confidence level; Fig. 6b).

469 Biotite-sillimanite gneiss (SO7). Data points are relatively scattered on the Th/Pb vs.
470 U/Pb diagram, leading to a small error envelope. The intercept ages are similar within errors,
471 since the intercept U-Pb age and the intercept Th-Pb age are at 331+39/-46 Ma, and 371+33/-
472 28 Ma, respectively. The calculated MSWD of 1.19 indicates that the population of 73
473 analyses is statistically homogeneous within the analytical errors (Wendt and Carl 1991) and
474 as a consequence, it is possible to calculate the mean age at the centroid. Thus, the monazite
475 grains yield a mean age of 355 ± 7 Ma (at 2σ confidence level; Fig. 6c).

476 Migmatitic gneiss (SO11) of Pont de Menat. Data points on the Th/Pb vs. U/Pb
477 diagram are less scattered than for previous sample, which may lead to a larger error envelop.
478 However, the large number of analyses (n= 174) decreases the envelop size. The intercept
479 ages are similar within errors, since the intercept U-Pb age and the intercept Th-Pb age are at
480 342+45/-51 Ma, and 373+24/-21 Ma, respectively. The calculated MSWD of 0.98 indicates
481 that the population of 174 analyses is statistically homogeneous within the analytical errors
482 (Wendt and Carl 1991). As a consequence, it is possible to calculate the mean age at the
483 centroid. Thus, the monazite grains yield a mean age of 363 ± 4 Ma (at 2σ confidence level;
484 Fig. 6d).

485 Kyanite-garnet granulitic paragneiss (SO15) of Saugères. Monazite in sample SO15
486 exhibits a core-rim zonation of the grain, and in consequence, EPMA data were processed
487 separately for the different domains in order to calculate two isochron ages. 47 and 21
488 analyses were performed in the core and rim of a single grain, respectively. The 47 analyses
489 from the core on the Th/Pb vs. U/Pb diagram are clustered, leading to a large error envelope.
490 The intercept ages are similar within errors, since the intercept U-Pb age and the intercept Th-
491 Pb age are at 517+281/-322 Ma, and 390+81/-57 Ma, respectively. The calculated MSWD of

1.15 indicates that the population of the 47 analyses is statistically homogeneous within the analytical errors (Wendt and Carl 1991). As a consequence, it is possible to calculate a mean age at the centroid. Thus, the core of this monazite grain yields a mean age of 416 ± 15 Ma (at 2σ confidence level; Fig. 6e).

Moreover, the 21 analyses performed from the monazite rim are well-scattered, leading to a small error envelope. The intercept ages are similar within errors, since the intercept U-Pb age and the intercept Th-Pb age are at 423+74/-88 Ma, and 338+36/-30 Ma, respectively. The calculated MSWD of 0.93 indicates that the population of 21 analyses is statistically homogeneous within the analytical errors (Wendt and Carl 1991). As a consequence, it is possible to calculate the mean age at the centroid where the precision is the best within the error envelope. Thus, the monazite grains yield a mean age of 362 ± 14 Ma (at 2σ confidence level; Fig. 6f).

Zircon U-Pb SIMS dating

Analytical procedure

Zircon concentrates were separated from a *ca* 5 kg of the granulitic paragneiss sample SO15 using standard density and magnetic separation techniques. Zircon grains, together with standard zircons TEMORA 2, 91500, and an in-house standard zircon Qinghu, were mounted in an epoxy mount that was then ground and polished to section the crystals in half for analysis. Zircons were imaged with transmitted and reflected light photomicrographs as well as cathodoluminescence (CL) to reveal their internal structures, and the mount was vacuum-coated with high-purity gold prior to SIMS analyses. Measurements of U, Th and Pb isotopes were conducted using a Cameca IMS 1280 SIMS at the Institute of Geology and Geophysics, Chinese Academy of Sciences in Beijing. Analytical procedures are similar to those reported by Li et al. (2009). The primary O_2^- ion beam spot is about 20×30 μm in size. Positive

secondary ions were extracted with a 10 kV potential. In the secondary ion beam optics, a 60 eV energy window was used, together with a mass resolution of *ca* 5400 (at 10% peak height), to separate Pb^+ peaks from isobaric interferences. A single electron multiplier was used in ion-counting mode to measure secondary ion beam intensities by peak jumping mode. Analyses of the standard zircon TEMORA 2 were interspersed with unknown grains. Each measurement consists of 7 cycles. Pb/U calibration was performed relative to zircon standard TEMORA 2 ($^{206}Pb/^{238}U$ age = 417 Ma, Black et al. 2004); U and Th concentrations were calibrated against zircon standard 91500 (Th = 29 ppm, and U = 81 ppm, Wiedenbeck and Allen 1995). Measured compositions were corrected for common Pb using non-radiogenic ^{204}Pb, and an average of crustal composition (Stacey and Kramers 1975) was used for the common Pb. Data reduction was carried out using the Isoplot/Ex v. 2.49 program (Ludwig 2001). In order to monitor the external uncertainties of SIMS U-Pb zircon measurements, an in-house standard zircon Qinghu was alternately analyzed as an unknown together with other unknowns. Twenty measurements on Qinghu zircon (Table 3) yield a Concordia age of 160 ± 1 Ma (2SE, MSWD of concordance = 0.92), which is in good agreement within errors with the recommended U-Pb age of 159.5 ± 0.2 Ma (Li et al. 2009). Zircon U-Pb age data are presented in Table 3.

Results

Fifty-five zircon grains from the SO 15 granulitic paragneiss have been analyzed (Table 3). All but four zircons are concordant within analytical uncertainties (discordance degree <4%). The dated zircons can be divided into two groups in terms of their morphological feature, ages and Th/U ratio. In group 1, zircons are mostly sub-rounded to multifaceted grains and yield ages between 324 and 349 Ma. They are characterized by low Th/U ratio (<0.1) and faint CL luminescence (Table 3, Fig. 7), similar to metamorphic zircons (Corfu et al. 2003). Contrarily,

Group 2 zircons are dated between 368 Ma and 1.99 Ga (Table 3). They are mostly oval shaped grains showing concentric zoning under CL (Fig. 7), and relatively high Th/U ratio (mostly >0.1), similar to the magmatic zircons (Corfu et al. 2003). Among them, four zircons (spots @06, 26, 27 and 37) are highly discordant, with $^{207}Pb/^{206}Pb$ ages between 1629 and 1994 Ma. On the probabilistic histogram of U-Pb ages for 51 concordant analyses (Fig 8), Group 1 zircons form one major peak at 342 Ma (n = 24) and a subordinate peak at 327 Ma (n = 6), corresponding to Concordia age of 343±2 Ma and 328±4 Ma, respectively, on a U-Pb Concordia plot (Fig. 9). Thus, Group 1 zircons are most likely metamorphic in origin. The remaining 21 Group 2 zircons display a scattered age pattern ranging from 370 to 800 Ma, which might be detritus zircons of magmatic origin with or without later metamorphic and hydrothermal overprinting.

Discussion

Many studies have pointed out the relationships between the age and the chemical composition of monazite grains in polymetamorphic terranes (e. g. Martins et al., 2009; Kelly et al., 2012). In samples SO3, SO7, SO11 and SO17, SEM BSE images of monazite grains revealed homogeneous grains. The chemical compositions of the analysed monazite grains cluster near the Monazite-(Ce) pole and scatter along the cheralite axis (Fig. 5a and b). The weak data dispersal along the cheralite substitution line indicates that the analysed grains represent a rather homogeneous population. Monazite grains from sample SO15 that exhibit a light (i.e. dense) core and a dark (i.e. light) rim in BSE images, are scattered between the cheralite ($CaTh(PO_4)_2$) and huttonite ($2ThSiO_4$) substitutions (Fig. 5b). Compared with the other analysed samples, such a difference is explained by a high REE (La, Ce, Pr, Nd) content and absence of Y in the core of monazite grains from sample SO15 (Table 2). The analysed spots in both the core and rim parts delimit two clusters with different chemical composition.

567 It is noteworthy that i) the chemistry of the SO15 monazite rim is close to the chemistry of the
568 other analysed monazite grains, and ii) the reaction leading to the rim crystallisation occurred
569 contemporaneously to the crystallisation of the other monazite grains in samples SO3, SO7,
570 SO11 and SO17. Datings carried out in this study have been made on grain populations with
571 homogeneous chemical composition that make us confident about the age interpretation.
572 The kyanite-garnet granulitic gneiss SO15 preserves a core domain within monazite
573 yielding a *ca* 415 Ma age. This Early Devonian age can be assigned to the D_0 event
574 recognized in the UGU in several places in the Massif Central (Pin and Peucat 1986; Pin and
575 Vielzeuf 1988; Paquette et al. 1995). All the dated samples, whatever the tectonic unit to
576 which they belong, yielded similar within the error, monazite U-Th-Pb ages at *ca* 365-350 Ma
577 (Fig. 10). Since they share common structural features, including a similar NW-SE striking,
578 D_2, stretching lineation, which is well developed in samples SO3, SO11, SO17, and SO15, the
579 363-351 Ma ages yielded by the monazite in these rocks can be attributed to the D_2 tectono-
580 metamorphic event. Similar ages were already reported for the D_2 tectono-metamorphic event
581 in other areas of the French Massif Central, such as the Lot series (Costa 1989) or Limousin
582 (Melleton et al. 2009). Moreover, these ages are consistent, within the errors, with the
583 emplacement age of the Guéret and S^t-Gervais d'Auvergne plutons (Figs 1, 2) that exhibit a
584 NW-SE striking magmatic lineation (Faure et al. 2005; Cartannaz et al. 2007). These plutons,
585 dated at 360-350 Ma, emplaced at the end of the D_2 event (Berthier et al. 1979; Cartannaz et
586 al. 2007; Faure et al., 2009). The SO11 D_1 migmatite sample, deformed during the D_2 event,
587 yields also a monazite U-Th-Pb age at *ca* 363 Ma, which is consistent with the Late
588 Devonian-Early Carboniferous age of the D_2 event.
589 It is worth to note that although the D_1 migmatization is preserved in samples SO11,
590 and SO7, the P-T conditions of 0.4-0.6 GPa and 550-600°C, calculated in the UGU from a
591 sample close to our sample SO7 (Schulz et al. 2001, Schulz 2009) are not in agreement with

592 the D_1 event, as defined in other areas of the French Massif Central (e.g. Santallier 1981;
593 Mercier et al. 1991; Lardeaux et al. 2001; Bellot and Roig 2007), but instead represent a low
594 pressure-medium temperature event similar to the D_2 one as observed in the Limousin, Lot or
595 Rouergue areas (Duguet et al. 2006; Bellot and Roig 2007; Melleton et al 2009). Thus this
596 biotite-sillimanite paragneiss might have also experienced the D_2 event, even if the typical
597 NW-SE D_2 stretching lineation is not observed in this rock. Furthermore, the NE-SW striking
598 D_1 mineral lineation is clearly observed in sample SO17. In these three rocks, the analyzed
599 monazites do not record the Devonian migmatization dated between 385 Ma and 375 Ma in
600 Lyonnais (Duthou et al. 1994), Limousin (Faure et al. 2008) and S. Brittany (Cocherie et al.
601 2005). This result can be variously interpreted. Firstly, monazite was unable to crystallize
602 under the D_1 metamorphic conditions; secondly, monazite effectively crystallized, but it may
603 have been dissolved during the HT event, and then neocrystallized in biotite during the
604 prograde D_2 event; thirdly, due to the limited number of analyzed grains, our sampling missed
605 any monazite grain formed during the D_1 event. Though the first hypothesis appears unlikely,
606 since aluminous composition protoliths are suitable for monazite crystallization, the other two
607 explanations cannot be discarded. Thus, the 365-350 Ma monazite ages obtained from
608 samples SO3, SO17, SO7, SO11, and the monazite rim from sample SO15 are attributed to
609 the neocrystallization or the complete recrystallization of monazite during the D_2 event,
610 leading to the total loss of any early monazite. In order to get a better understanding of the
611 thermo-barometric and chemical conditions that allow monazite crystallization or dissolution
612 with respect to other phases such as garnet and biotite, a detailed analysis of the chemical
613 elements exchanges during the succession of the crystallization-deformation events would be
614 necessary. On the contrary to Limousin or Maures areas (e. g. Duguet et al. 2006; Bellot and
615 Roig 2007; Oliot et al. 2015), such a study is not available yet for the Sioule metamorphic
616 series.

Besides, zircon from the granulitic paragneiss yields U-Pb SIMS ages younger than the monazite ones at 343±2 Ma, and 328±2 Ma. The latest is close to the whole-rock Rb/Sr age of the Pouzol-Servant microgranite at 330 Ma (Duthou and Pin 1987; Pin 1991), and also to the cooling ages yielded by the $^{40}Ar/^{39}Ar$ analyses on biotite, muscovite and amphibole for the entire nappe-stack of the Sioule metamorphic series, either in the Upper Gneiss, Lower Gneiss, and Para-autochthonous Units (Faure et al. 2002; Fig. 11). As pointed out in the "Geological Setting" section, the *ca* 330 Ma age is that of the "Tufs anthracifères" magmatism widespread in the northern part of the French Massif Central (Fig. 11). The $^{40}Ar/^{39}Ar$ ages of the Sioule metamorphic rocks, younger than the Late Visean unconformity, have been interpreted as a thermal reset provided by the high heat flux during the onset on the extensional tectonics in the northern part of the French Massif Central. Thus we suggest here that the zircon age at 328±4 Ma Ma might be due to recrystallizations processes, possibly assisted by hydrothermal fluids, also as a consequence of the Late Visean thermal reset. Indeed, the LGU and PAU rocks exhibit several evidence of retrogression such as chlorite developed at the expense of biotite, sericite surrounding staurolite, (Fig 4a) and albite overprinting the foliation. These minerals argue for a late metamorphic stage associated with fluid circulation. In the present state of knowledge, detailed petrological investigations to characterize this hydrothermal event are not available. The 343±2 Ma age yielded by 24 zircon grains is more difficult to interpret in the geological framework. This age corresponding to the majority of analyzed concordant grains is different, within the error, from the 328±4 Ma age. Furthermore, such a Middle Visean age is rarely reported in the northern part of the Massif Central. However, to the East of the study area, in the Lyonnais, syn-kinematic granites emplaced along a NE-SW striking dextral strike-slip fault yield biotite and muscovite $^{40}Ar/^{39}Ar$ ages at ca 346±3 Ma and 349±3 Ma, respectively (Costa et al. 1993). Such a NE-SW strike-slip shearing is not identified in the Sioule area, but the NW-SE striking

642 S^{te}-Christine dextral strike slip fault develops in the southern boundary of the Sioule series
643 (Fig. 2). One possible interpretation would be to relate this *ca* 343 Ma (i. e. Middle Visean)
644 age to fluid circulations coeval with a transcurrent shearing event too. Importantly, the zircon
645 SIMS measurement did not recorded the 365-350 Ma D_2 ages.

646 Previous monazite U-Th/Pb ages (Schulz 2009) range between 343 Ma and 327 Ma,
647 i.e. much younger than those reported in this study. These dates were attributed to two distinct
648 events, in agreement with the $^{40}Ar/^{39}Ar$ ages (Faure et al. 2002), the monazite chemical ages
649 younger than 340 Ma were considered as due to the Late Visean hydrothermal event related to
650 the "Tufs anthracifères" magmatism. Conversely, ages older than 340 Ma were considered as
651 minimum ones associated to a top-to-the-SE tectonic event. However, structural
652 investigations demonstrated that the top-to-the-SE shearing was coeval with the emplacement
653 of the Echassières pluton at *ca* 310 Ma (Feybesse and Teygey 1987; Faure et al. 1993). The
654 discrepancy between our results and the previous ages by Schulz (2009) can also be explained
655 considering the data reduction method. The previous study uses frequency histograms to
656 process the analytical data associated with very large, routinely *ca* 15 Ma, errors. Moreover,
657 the frequency diagram method provides a mean age systematically younger than the one given
658 by the Th/Pb= f(U/Pb) isochron method (Cocherie and Albarède 2001). For example, the
659 weighted average age computed here for the monazite core and rim of sample SO15 (Fig. 5c)
660 also yields ages at 392±16 Ma, and 359±18 Ma younger than 416±8 Ma, and 362±14 Ma
661 yielded by the isochron method. In addition, the results provided by the isochron method are
662 generally closer to the ICP-MS isotopic measurements than those provided by the histogram
663 method (Cocherie et al. 1998; Cocherie and Albarède 2001), and thus are preferred here. As
664 mentionned in the "Sioule metamorphic series" section, in the study area, two pre-Late Visean
665 events, namely D_1 and D_2, are recognized. However, the age of the D_1 and D_2 range between

385-375 Ma and 360-350 Ma, respectively. Therefore, the *ca* 340 Ma monazite ages cannot be ascribed to a single tectono-metamorphic event.

Our new monazite chemical ages can be used to place time constraints in the pressure (P)-temperature (T) plot in order to settle the P-T-t paths experienced by each unit. P-T estimates from the Sioule area (Schulz et al. 2001) are consistent with P-T conditions from other areas of the Massif Central (e.g. Santallier 1981; Mercier et al. 1991; Lardeaux et al. 2001; Bellot and Roig 2007; Faure et al. 2008). The UGU, LGU, and PAU underwent different P-T paths depending on their location in the French Massif Central. In the Lyonnais area, the coesite bearing eclogite argue for P conditions about 2.7-2.8 GPa (Lardeaux et al. 2001) whereas such ultra-high pressure conditions are not recorded (or not preserved) in the Sioule area. On the basis of petrological studies in the Limousin and Artense areas (Santallier 1981, Mercier et al. 1991), peak-conditions of *ca* 2 GPa for *ca* 800°C are inferred for the Sioule granulite (Fig. 12). Sample SO15 places a time constraint at *ca* 415 Ma on this HP event. On the contrary, in the Limousin area, the LGU reached a maximum P value of 1.1-1.2 GPa for 500 °C (Bellot and Roig 2007; Faure et al. 2008). During their exhumation, the UGU and LGU followed nearly isothermal decompression paths coeval with migmatization, and subsequent cooling during the D_1 event at 385-375 Ma. The minimum P-T conditions experienced by the UGU and LGU during this eo-Variscan cycle are not precisely settled. Since andalusite replacing sillimanite or kyanite is never observed in the UGU or LGU, we assume that the two units were not exhumed close to the surface but remained burried in the upper crust, even if aluminosilicates might have remained stable during exhumation. Conversely, the PAU never experienced the D_1 metamorphism nor migmatization. This unit records maximum P and T values of 0.7-0.8 GPa, and 500-600°C, respectively. Our monazite age of sample SO3 at 363±8 Ma constrains the age of the MP/MT metamorphism coeval with the top-to-the-NW D_2 event. During the same late Devonian-Early Carboniferous period, the

691 UGU and LGU experienced a second metamorphic cycle leading to maximum P-T conditions
692 of 0.7-0.8 GPa, and 500-600°C similar to those of the PAU. Our monazite U-Th-Pb ages at
693 362Ma, 363 Ma, 355 Ma, and 351 Ma, for samples SO10, SO11, SO7, and SO17,
694 respectively represent the age of the D_2 event recorded in the UGU and LGU (Fig. 12).
695 After the completion of the two Variscan metamorphic cycles, the Sioule metamorphic
696 series, like most of the areas in the northern part of the FMC, experienced a huge late
697 orogenic magmatic episode, at *ca* 335-330 Ma, represented both by deep seated plutonism,
698 dyke emplacement, and aerial volcanism. As already proposed to account for the $^{40}Ar/^{39}Ar$
699 ages, the hydrothermalism was responsible for the complete resetting of the zircon U-Pb
700 isotopic systems during the Tufs Anthracifères event but the U-Th-Pb chronometer was not
701 affected by this late thermal event.
702
703 **Conclusion**
704 This geochronological study in a key area of the Variscan French Massif Central, casts light
705 on the importance of structural and petrological constraints when dealing with age
706 determination of thermal, tectonic and metamorphic events in orogens. These new radiometric
707 ages yielded by monazite and zircon included in the macroscopic foliation allow us to place
708 time constraints on the succession of superimposed deformation and related metamorphic
709 events in the Sioule area. The early Variscan HP/HT D_0 event occurred at 416±15 Ma and the
710 MP/MT D_2 event, coeval with the top-to-the NW shearing took place between 365 Ma and
711 350 Ma. On the contrary, the *ca* 380 Ma D_1 event has not been recorded by monazite. Our
712 study emphasizes that radiometric ages must be carefully discussed in the light of the regional
713 geological setting. Particularly, the knowledge of the thermo-barometric and hydrothermal
714 processes must be a pre-requisite for the understanding of the geochronological data.
715
716 **Acknowledgements**

717 Field, and analytical expenses for this study have been supported by the French national
718 program “Carte géologique de la France au 1/50 000" led in BRGM, and by a National
719 Natural Science Foundation of China (NNSFC) grant 41273070. Ida di Carlo and Olivier
720 Rouer are acknowledged for their help for the acquisition of SEM and EPMA analyses. Jean-
721 Marc Lardeaux and Emilien Oliot are thanked for their constructive reviews.

722

723 **References**

724 Bé Mézème E, Cocherie A, Faure M, Legendre O, Rossi P (2006) Electron microprobe
725 monazite geochronology: a tool for evaluating magmatic age domains. Examples
726 from the Variscan French Massif Central. Lithos 87: 276–288

727

728 Bellot J-P, Roig J-Y (2007) Episodic exhumation of HP rocks inferred from structural data
729 and P-T paths from the southwestern part Massif Central (Variscan belt, France). J Struct
730 Geol 29: 1538-1557

731

732 Berger J, Féménias O, Ohnenstetter D, Bruguier O, Plissart G, Mercier JC, Demaiffe D
733 (2010) New occurrence of UHP eclogites in Limousin (French Massif Central): Age, tectonic
734 setting and fluid–rock interactions. Lithos 118: 365-382.

735

736 Berthier F, Duthou JL, Roques M, (1979) Datation géochronologique Rb/Sr sur roches totales
737 du granite de Guéret (Massif central). Âge fini-Dévonien de mise en place de l’un de ses
738 faciès types. Bull. Bur. Rech. Geol. Min. I : 31–42.

739

740 Black LP, Kamo SL, Allen, CM, Davis D, Aleinikoff JN, Valley JW, Mundil R, Campbell IH,
741 Korsch RJ, Williams IS, Foudoulis C (2004) Improved $^{206}Pb/^{238}U$ microprobe geochronology

742 by the monitoring of a trace-element-related matrix effect; SHRIMP, ID-TIMS, ELA-ICP-MS
743 and oxygen isotope documentation for a series of zircon standards. Chemical Geology 205 :
744 115–140
745
746 Boutin R, Montigny R, (1993) Datation $^{39}Ar/^{40}Ar$ des amphibolites du complexe leptyno-
747 amphibolique du plateau d'Aigurande : collision varisque à 390 Ma dans le Nord-Ouest du
748 Massif central français. C. R. Acad. Sci. Paris Ser. II 316 : 1391–1398
749
750 Bruguier O, Becq-Giraudon JF, Bosch D, Lancelot JR, (1998) Late Visean (Upper
751 Missisipian) hidden basins in the internal zones of the Variscan Belt: U-Pb zircon evidence
752 from the French Massif Central. Geology 26 : 627–630
753
754 Cabella R, Lucchetti G, Marescotti P (2001) Authigenic monazite and xenotime from pelitic
755 metachert in pumpellyite-actinolite facies conditions, Sestri-Voltaggio zone, Central Liguria,
756 Italy. The Canadian Mineralogist 39 : 717-727
757
758 Caron C, (1994) Les minéralisations Pb-Zn associées au Paléozoïque inférieur d'Europe
759 méridionale. Traçage isotopique Pb-Pb des gîtes de l'Iglesiente (SW Sardaigne) et des
760 Cévennes et évolution de socle encaissant par la géochronologie U-Pb, ^{40}Ar-^{39}Ar et KAr
761 Thèse, Univ. Montpellier, 288 pp
762
763 Cartannaz C, Rolin P, Cocherie A, Marquer D, Legendre O, Fanning C M, Rossi P (2007)
764 Characterization of wrench tectonics from dating of syn- to post-magmatism in the
765 northwestern French Massif Central. Int J Earth Sci 96 : 271-287
766

767 Cheilletz A, Archibald DA, Cuney M, Charoy B (1992) Ages $^{40}Ar/^{39}Ar$ du leucogranite à
768 topaze-lépidolithe de Beauvoir et des pegmatites sodomithiques de Chédeville (Nord du
769 Massif Central, France). Compte Rendus Acad Sci Paris 315 : 329-336
770
771 Cocherie A, Albarède F (2001) An improved U-Th-Pb age calculation for electron
772 microprobe dating of monazite. Geochimica Cosmochimica Acta 65 : 4509-4522
773
774 Cocherie, A., Legendre O (2007) Potential minerals for determining U-Th-Pb chemical age
775 using electron microprobe. Lithos 93 : 288–309
776
777 Cocherie A, Legendre O, Peucat J J, Kouamelan AN (1998) Geochronology of
778 polygenetic monazites constained by in situ electron microprobe Th–U–total Pb
779 determination: implications for lead behaviour in monazite. Geochimica Cosmochimica
780 Acta 62 : 2475–2497
781
782 Cocherie A, Bé Mézème E, Legendre O, Fanning M, Faure M, Rossi P (2005) Electron
783 microprobe dating as a tool for understanding closure of U-Th-Pb system in monazite from
784 migmatite. Am Mineralogist 90 : 607-618
785
786 Cocks LRM (2000) The Early Paleozoic geography of Europe. J Geol Soc London 157: 1-10
787
788 Corfu F, Hanchar JM, Hoskin PWO, Kinny P (2003) Atlas of Zircon Textures. In: Hanchar,
789 J.M., Hoskin, P.W.O. (Eds.), Zircon. Reviews in Mineralogy and Geochemistry 53: 469-500.
790
791

792 Costa S, (1989) Age radiométrique 40Ar/39Ar du métamorphisme des séries du Lot et du
793 charriage du groupe leptyno-amphibolique de Marvejols (Massif central français), C. R. Acad.
794 Sci. Paris Ser. II 309 : 561–567
795
796 Costa S, Maluski S, Lardeaux J-M (1993) $^{40}Ar/^{39}Ar$ chronology of Variscan tectono-
797 metamorphic events in an exhumed crustal nappe: the Monts du Lyonnais complex (Massif
798 Central, France). Chemical Geology 105: 339-359
799
800 Costa S, Maluski S (1988) Datations par la méthode $^{40}Ar/^{39}Ar$ de matériel magmatique et
801 métamorphique paléozoïque provenant du forage de Couy-Sancerre (Cher, France)
802 Programme GPF. C R Acad Sci Paris Ser II 306 : 351–356
803
804 Duguet M, Le Breton N, Faure M (2006) P-T paths reconstruction of a collisional event: the
805 example of the Thiviers-Payzac Unit in the Variscan French Massif Central Lithos 98 : 210–
806 232
807
808 Duthou JL, Cantagrel JM, Didier J, Vialette Y (1984) Paleozoic granitoids from the French
809 Massif Central: age and origin studied by $^{87}Rb/^{87}Sr$ system. Phys Earth Planet Int 35: 131-144
810
811 Duthou JL, Pin C (1987) Etude isotopique Rb-Sr de l'apex granitique d'Echassières. Géologie
812 de la France 2 : 63-67
813
814 Duthou JL, Chenevoy M, Gay M (1994) Age Rb/Sr Dévonien moyen des migmatittes à
815 cordiérite du Lyonnais (Massif central français). Comptes Rendus
816 de l'Académie des Sciences 319 : 791–796

817

818 Faure M, Grolier J, Pons J (1993) Extensional ductile tectonics of the Sioule metamorphic
819 series (Variscan French Massif Central). Geol. Rundschau 82: 461-474

820

821 Faure M (1995) Late orogenic Carboniferous extensions in the Variscan French Massif
822 Central. Tectonics 14 : 132–153.

823

824 Faure M, Leloix C, Roig JY, (1997) L'évolution polycyclique de la chaîne hercynienne. Bull.
825 Soc. Geol. France 168: 695-705

826

827 Faure M, Monié P, Maluski H, Pin C, Leloix C (2002) Late Visean thermal event in the
828 northern part of the French Massif Central. New $^{40}Ar/^{39}Ar$ and Rb-Sr isotopic constraints on
829 the Hercynian syn-orogenic extension. Int. J. Earth Sciences 91: 53-75

830

831 Faure M, Bé Mézème E, Duguet M, Cartier C, Talbot J-Y (2005) Paleozoic tectonic evolution
832 of Medio-Europa from the example of the French Massif Central and Massif Armoricain. J
833 Virtual Explorer Electronic edition ISSN 1441-8142, 19 paper 5.

834

835 Faure M, Bé Mézème E, Cocherie A, Rossi P, Chemenda A, Boutelier D (2008) Devonian
836 geodynamic evolution of the Variscan Belt, insights from the French Massif Central and
837 Massif Armoricain. Tectonics 27: TC2008, http://dx.doi.org/10.1029/2007TC002115

838

839 Faure M, Lardeaux JM, Ledru P (2009) A review of the pre-Permian geology of the French
840 Massif Central. Comptes Rendus Géosciences, thematic issue « The Variscan Orogeny » 341:
841 202-213 doi :10.1016/j.crte.2008.12. 001

Faure M, Cocherie A, Bé-Mézème E, Charles N, Rossi P (2010) Middle Carboniferous crustal melting in the Variscan Belt: New insights from U-Th-Pb_{tot}. monazite and U-Pb zircon ages of the Montagne Noire Axial Zone (southern French Massif Central). Gondwana Research 633-673. doi 10.1016/j.gr.2010.02. 005.

Feybesse JL, Teygey M (1987) Evolution tectonométamorphique dévonienne de la série de la Sioule. Géologie de la France 2 : 33-41

Franz G, Andrehs G, Rhede D (1996) Crystal chemistry of monazite and xenotime from Saxothuringian-Moldanubian metapelites, NE Bavaria, Germany European J Mineralogy 8 : 1097-1118

Grolier J (1971) Contribution à l'étude géologique des séries crystallophylliennes inverses du massif Central français: la série de la Sioule (Puy de Dôme, Allier). Mem BRGM 64, 163pp.

Janots E, Negro F, Brunet F, Goffé B, Engi M, Bouybaouène ML (2006) Evolution of REE mineralogy in HP-LT metapelites of the Sebtides complex, Rif, Morocco: Monazite stability and geochronology. Lithos 87: 214-234

Jourdan F, Mark D, Verrati C (2014) Advances in $^{40}Ar/^{39}Ar$ dating: from archaeology to planetary sciences – introduction. Jourdan, F., Mark, D. F. & Verati, C. (eds) 2014. Advances in 40Ar/39Ar Dating: from Archaeology to Planetary Sciences. Geological Society, London, Special Publications 378: 1–8

867 Joly A, Chen Y, Faure M, Martelet G (2007) A multidisciplinary study of a syntectonic pluton
868 close to a major lithospheric-scale fault: relationships between the Montmarault granitic
869 massif and the Sillon Houiller Fault in the Variscan French Massif Central. Part I:
870 Geochronology, mineral fabrics and tectonic implications. J. Geophys. Res., 112, B10104,
871 http://dx.doi.org/10.1029/2006JB004745
872
873 Kelly N.M, Harley S.L, Möller A, (2012) Complexity in the behavior and recrystallization of
874 monazite during high-T metamorphism and fluid infiltration. Chemical Geology 322–323 :
875 192-208
876
877 Kohn JM, Malloy MA (2004) Formation of monazite via prograde metamorphic reactions
878 among common silicates: implications for age determinations. Geochimica Cosmochimica
879 Acta 68: 101-113
880
881 Lardeaux JM, Ledru P, Daniel I, Duchène S (2001) The Variscan French Massif Central – a
882 new addition to the ultra-high pressure metamorphic ‘‘club’’: exhumation processes and
883 geodynamic consequences. Tectonophysics 323 : 143–167
884
885 Lardeaux JM, Schulmann K, Faure M, Janousek V, Lexa O, Skrzypek E, Edel J-B, Stipska P
886 (2014) The Moldanubian Zone in French Massif Central, Vosges/Schwarzwald and Bohemian
887 Massif revisited: Differences and similarities. In « *The Variscan Orogeny: Extent, Timescale*
888 *and the Formation of the European Crust* ». Schulmann K, Martínez Catalán J R, Lardeaux J
889 M, Janousek V & Oggiano G (eds). Geological Society, London, Special Publications 405:
890 http://dx.doi.org/10.1144/SP405.14
891

892 Ledru P, Lardeaux JM, Santallier D, Autran A, Quenardel JM, Floc'h JP, Lerouge G, Maillet
893 N, Marchand J, Ploquin A (1989) Où sont les nappes dans le Massif central français ? Bull.
894 Soc. Géol. France 8 : 605–618
895
896 Leloix C, Faure M, Feybesse JL, (1999) Hercynian polyphase tectonics in north-east French
897 Massif Central : the closure of the Brévenne Devonian-Dinantian rift. Int. J. Earth. Sci. 88:
898 409-421
899
900 Li XH, Liu Y, Li QL, Guo CH (2009) Precise determination of Phanerozoic zircon Pb/Pb age
901 by multicollector SIMS without external standardization. Geochemistry Geophysics
902 Geosystems 10 : Q04010, http://dx.doi.org/10.1029/2009GC002400
903
904 Linthout K (2007) Tripartite division of the system $2REEPO_4$-$CaTh(PO4)_2$ -$2ThSiO_4$,
905 Discreditation of Brabantite, and recognition of Cheraliteas the name for members dominated
906 by $CaTh(PO4)_2$. The Canadian Mineralogist 45 : 503-508
907
908 Ludwig KR (2001) ISOPLOT/EX, version 2.49. A geochronological toolkit for Microsoft
909 Excel. Berkeley Geochronology Center, Berkeley, Special Publications, 4
910
911 Martins L, Farias Vlach S.R, Janasi VdA, (2009) Reaction microtextures of monazite:
912 Correlation between chemical and age domains in the Nazaré Paulista migmatite, SE Brazil.
913 Chemical Geology 261 : 271-285
914
915

916 Matte P (1986) Tectonic and plate tectonic model for the Variscan belt of Europe.
917 Tectonophysics 126: 329-374
918
919 Matte P. (2001) The Variscan collage and orogeny (480–290 Ma) and the tectonic definition
920 of the Armorica microplate. Terra Nova 13: 122–128
921
922 Mc Farlane CRM, Frost BR (2009) Constraints on the early metamorphic evolution of
923 Broken Hill Australia, from in situ U-Pb dating and REE geochemistry of monazite. J
924 Metamorphic Geology 27: 3-17
925
926 Melleton J, Faure M, Cocherie A, (2009) Monazite U-Th/Pb chemical dating of the Early
927 Carboniferous syn-kinematic MP/MT metamorphism in the Variscan French Massif Central.
928 Bull. Soc. Géol. France 180: 283-292.
929
930 Melleton J, Gloaguen E, Frei D, Lima A (2011) U-Pb dating of columbite-tantalite from
931 Variscan rare-elements granites and pegmatites. Goldschmidt Conference Abstracts Min.
932 Mag. 75: 1432.
933
934 Mercier L, Lardeaux JM, Davy P (1991) On the tectonic significance of the retromorphic P-T
935 paths of the French Massif Central eclogites. Tectonics 10 : 131–140
936
937 Montel J.M, Foret S, Veschambre M, Nicollet C, Provost A (1996) Electron microprobe
938 dating of monazite. Chem Geol 131 : 37–53
939

940 Murphy B, Cousens B, Braid L, Strachan R, Dostal J, Keppie D, Nance D (2011) Highly
941 depleted oceanic lithosphere in the Rheic Ocean: Implications for Paleozoic plate
942 reconstructions. Lithos, 123: 165-175
943
944 Nagy G, Draganits E, Demeny A, Panto G, Arkai P (2002) Genesis and transformations of
945 monazite, florencite and rhabdophane during medium grade metamorphism : examples from
946 the Sopron Hills, Eastern Alps. Chem Geol 191 : 25-46
947
948 Olliot E, Melleton J, Schneider J, Corsini M, Gardien V, Rolland Y (2015) Variscan crustal
949 thickening in the Maures-Tanneron massif (South Variscan belt, France): new in situ
950 monazite U-Th-Pb chemical dating of high-grade rocks. Bull. Soc. Géol France 186: 145-169.
951
952 Parrish R (1990) U–Pb dating of monazite and its application to geological problems.
953 Canadian Journal of Earth Sciences 27 : 1431–1450
954
955 Paquette JL, Monchoux P, Couturier JP (1995) Geochemical and isotopic study of a norite-
956 eclogite transition in the EuropeanVariscan belt: implication for U–Pb zircon systematics in
957 metabasic rocks. Geochimica Cosmochimica Acta 59 : 1611–1622.
958
959 Pin C, Peucat J-J (1986) Ages des épisodes de métamorphisme paléozoïques dans le Massif
960 central et le Massif armoricain. Bull Soc Géol France 8: 461–469.
961
962 Pin C, Vielzeuf D (1988) Les granulites de haute pression d'Europe moyenne témoins d'une
963 subduction éo-hercynienne. Implication sur l'origine des groupes leptyno-amphiboliques. Bull
964 Soc Géol France 4: 13-20
965

966 Pin C (1990) Variscan oceans: ages, origins and geodynamic implications inferred from
967 geochemical and radiometric data. Tectonophysics 177 : 215–227
968
969 Pin C (1991) Sr-Nd isotopic study of igneous and metasedimentary enclaves in some
970 Hercynian granitoids from the Massif Central, France In : Didier J, Barbarin B (eds)
971 Developments in Petrology 13 Enclaves and granite petrology Elsevier Amsterdam 333-343
972
973 Pommier A, Cocherie A, Legendre O (2002) EPMA Dating User's manual: age calculation
974 from electron probe microanalyser measurements of U–Th–Pb. Bureau de Recherches
975 Géologiques et Minières (BRGM), 9.
976
977 Rasmussen B, Fletcher IR, Mc Naughton NJ (2001) Dating low-grade metamorphic events by
978 SHRIMP U-Pb analysis of monazite in shales. Geology 29 : 963-966
979
980 Ravier J, Chenevoy M (1979) Présence de formations granulitiques jalonnant un linéament
981 crustal dans la série crystallophyllienne de la Sioule (Massif central français). Comptes
982 Rendus Acad Sci II 288 : 1703-1706
983
984 Richard J (1938) Etude de la série cristallophyllienne renversée de la Sioule. Revue Sci.
985 Naturelles de la Haute Auvergne 4, 1: 37pp
986
987 Roig JY, Faure M (2000) La tectonique cisaillante polyphasée du Sud-Limousin. Bull. Soc.
988 Géol. France 171: 295-307
989

990 Santallier N (1981) Les roches basiques de la série métamorphique du Bas-Limousin, Massif
991 Central (France), Thèse, Univ. Orléans, France, 350 pp
992
993 Schulz B, Triboulet C, Audren C, Feybesse JL (2001) P-T paths from metapelite garnet
994 zonations, and crustal stacking in the Variscan inverted metamorphic sequence of La Sioule,
995 French Massif Central. Z dt Geol Ges 152 : 1-25
996
997 Schulz B (2009) EMP-monazite age controls on P-T paths of garnet metapelites in the
998 Variscan inverted metamorphic sequence of La Sioule, French Massif Central. Bull. Soc.
999 Géol. Fr. 180 : 271-282
1000
1001 Smith HA, Barreiro B (1990) Monazite U-Pb dating of staurolite grade metamorphism in
1002 pelitic schists. Contribution Mineral Petrol 105 : 602-615
1003
1004 Stacey JS, Kramers JD (1975) Approximation of terrestrial lead isotope evolution by a two-
1005 stage model. Earth and Planetary Science Letters 26 : 207–221
1006
1007 Suzuki K, Adachi M (1991) Precambrian provenance and Silurian metamorphism of the
1008 Tsubonosawa paragneiss in the South Kitakami terrane, Northeast Japan, revealed by the
1009 chemical Th-U-total Pb isochron ages of monazite, zircon and xenotime. Geochem J 25 : 357-
1010 376
1011
1012 Talbot JY, Faure M, Chen Y, Martelet G, (2005) Pull apart emplacement of the Margeride
1013 granitic complex (French Massif Central). Implications for the Late evolution of the Variscan
1014 orogen. J. Struct. Geol. 27: 1610-1629

Wendt I, Carl C (1991) The statistical distribution of the mean squared weighted deviation. Chem Geol 86 : 275-285

Wiedenbeck M, Allen P, 1995. Three natural zircon standards for U–Th–Pb, Lu-Hf, trace element and REE analysis. Geostandards Newsletter 19 : 1–23

Figure Captions

Fig. 1. A: Location of the French Massif Central in the European Variscan framework. B: Structural map of the Massif Central (modified from Ledru et al., 1989, and Faure et al., 2009). D_1, D_2, D_3 refer to the stretching lineation and kinematics referred to the Early Devonian, Early Carboniferous, and Middle Carboniferous tectono-metamorphic events, respectively. SGA: S^t-Gervais d'Auvergne pluton

Fig. 2. Structural map, and NW-SE cross-section of the Sioule series with sampling sites and microstructural data, after Grolier (1971), Feybesse and Teygey (1987), and Faure et al. (1993).

Fig. 3. Examples of representative macroscopic field structures of the Para-autochthonous (a), Lower Gneiss (b) and Upper Gneiss (c, d) Units. a1: outcrop of biotite-staurolite micaschist of sample SO3, with top-to-the-SE sigmoidal quart veins, a2: close-up of the mineral lineation marked by elongated biotite and staurolite porphyroblasts. This NW-SE lineation results of the superposition of D_2 and D_4 events. b) D1 NE-SW striking isoclinal folds at Chouvigny. c)

Biotite-sillimanite paragneiss with S1 flat-lying foliation and L1 mineral lineation, close to sample SO7. d) hand sample of garnet-kyanite granulitic paragneiss at Saugères (sample SO 15). Note the biotite rim around garnet developed during the retrogression of the granulite facies metamorphic assemblage into ampohibolite facies ones.

Fig. 4. Polarized light micrographs of analyzed samples showing the textural relationships of the dated monazite grains with other minerals (see location in Fig. 2). a: PAU micaschist sample SO3 from the Para-autochthonous Unit showing D_2 staurolite mantled by a sericite rim and deformed during the D_4 event. b: biotite-garnet-sillimanite gneiss (sample SO7) from the Upper Gneiss Unit with monazite included in biotite. c: biotite-sillimanite migmatite (sample SO11) foliated and lineated during the D_2 event, the dated monazite is included in biotite. d: kyanite-garnet granulitic paragneiss (sample SO15) with garnet surrounded by a biotite rim developed during the D_2 event.

Fig. 5. a: plot of the analyzed monazites in the $2REEPO_4$-$CaTh(PO_4)_2$-$2ThSIO_4$ system (Linthout, 2007) showing that the grains are close to the Ce-monazite pole. b: plot of the analyzed monazite in the Th+U+Si+Pb vs REE+P diagram (Franz et al., 1996). c: weighted average age of the core and rim of monazite contained in kyanite-garnet paragneiss of Saugères (sample SO15). d: X-ray compositional map for Th, Ca, U of the analyzed monazite grain in the granulitic paragneiss sample SO15, showing the chemical zoning with a Th, Ca, and U enriched rim. White and black squares represent EPMA analyse points for core and rim, respectively.

Fig. 6. Th/Pb vs U/Pb plots with SEM BSE pictures of dated monazites, sample location shown on Fig. 2, and GPS in Table 1. a, b, c, b: Upper Gneiss Unit. a) core of monazite grain

from SO 15 granulite (Saugères); b) rim of monazite grain from SO15 granulite (Saugères); c) biotite-sillimanite migmatitic gneiss SO11 from Pont de Menat; d) biotite-sillimanite migmatitic paragneiss SO7 from Moulin de Bouchet; e) biotite-staurolite micaschist SO3 from the Para-autochthonous Unit; f) two-mica paragneiss SO17 from the Lower Gneiss Unit.

Fig. 7. Cathodoluminescence (CL) images for representative zircons sample SO 15. The white ellipses in the CL images represent the spots of SIMS U-Pb analysis. SIMS spots are 30 μm in length for scale.

Fig. 8. Probability histogram of U-Pb age for 51 concordant analyses showing the two groups of zircon ages. Group 1 zircons have a main peak at 342 Ma and a secondary one at 327 Ma.

Fig. 9. Zircon U-Pb Concordia age of granulitic paragneiss sample S015.

Fig. 10. Synthetic map summarizing the available radiometric ages obtained through different methods, whole rock Rb/Sr, biotite and muscovite $^{40}Ar/^{39}Ar$, monazite U-Th-Pb, and zircon U-Pb SIMS for the Sioule series.

Fig. 11. Synoptic chart of the radiometric ages from the Sioule series presented in this paper, compared with the ages of the D_1, D_2, D_3 tectono-thermal events for the French Massif central, and the Guéret and S^t-Gervais biotite granites, and Pouzol-Servant microgranite. (1): Average biotite,muscovite, and hornblende $^{40}Ar/^{39}Ar$ ages from Faure et al. (2002); (2): zircon U-Pb age of the Pouzol-Servant microganite (Pin 1991); (3): zircon U-Pb SHRIMP and monazite U-Th-Pb chemical ages of the Guéret-St-Gervais plutons (Cartannaz et al. 2007).

Fig. 12. P-T-t paths for the Upper Gneiss Unit (UGU), Lower Gneiss Unit (LGU), and Para-Autochthonous Unit (PAU) modified from Mercier et al. 1991, Lardeaux et al., 2001; Schulz et al., 2001; Bellot and Roig 2007; Faure et al. 2007; Schulz 2009) emphasizing the polycyclic evolution. During the eo-Variscan cycle, the UGU experienced the D_0 high to ultra-high pressure metamorphism, and Devonian migmatization during its D_1 exhumation. The LGU underwent burial under lower pressure conditions than the UGU, then Devonian exhumation and migmatization during D_1. During the Late Devonian-Early Carboniferous D_2 event, the PAU followed its first burial and exhumation cycle, whereas the LGU and UGU experienced a second metamorphic cycle before its Late Visean exhumation.

Table 1. Dated sample locations and analytical data

Table 2. Electron microprobe analyses of dated monazites

Table 3. Zircon U-Pb zircon analyses of granulitic paragneiss sample SO15

Figure 1
Click here to download high resolution image

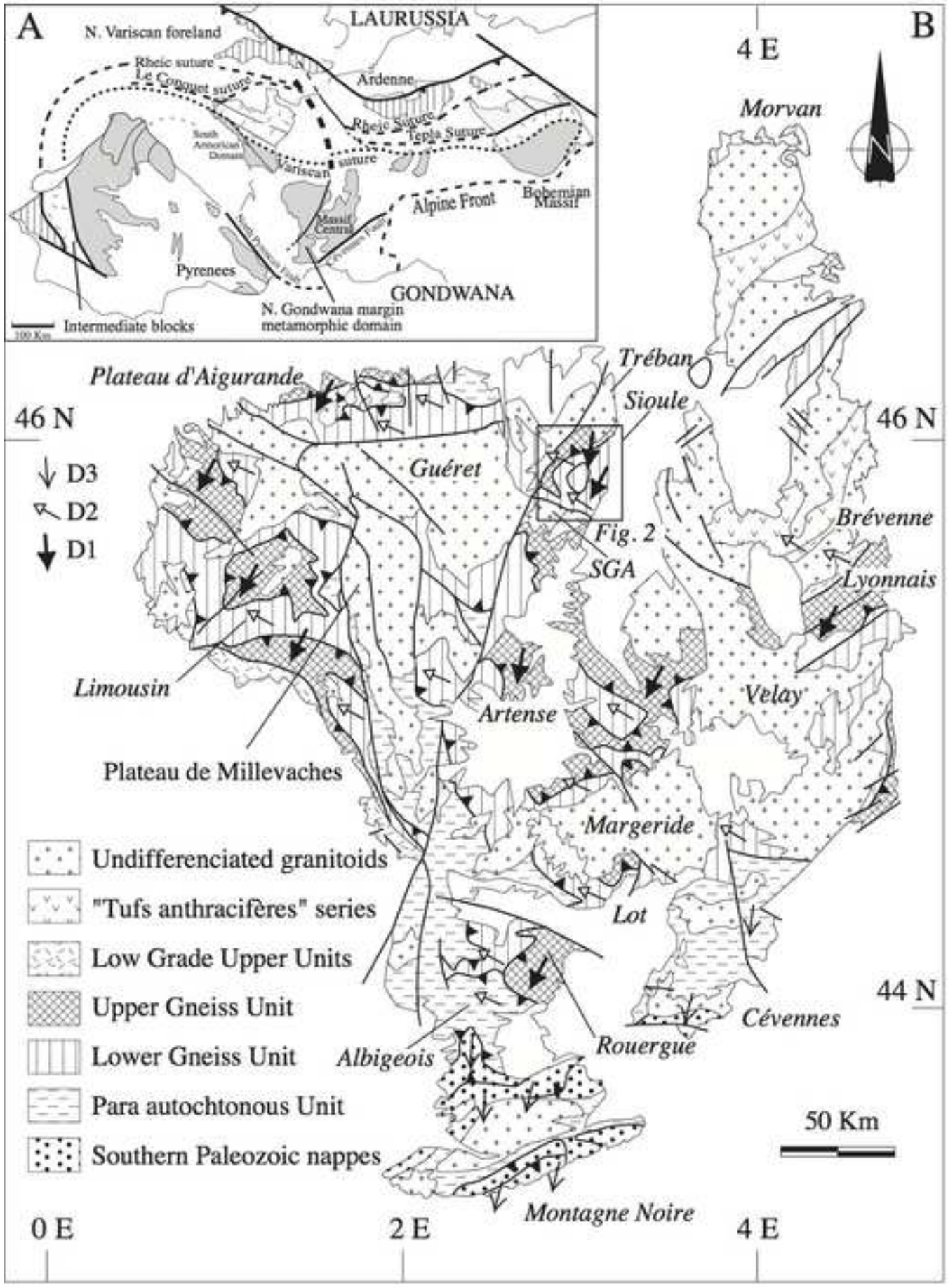

Fig. 1

Figure 2
Click here to download high resolution image

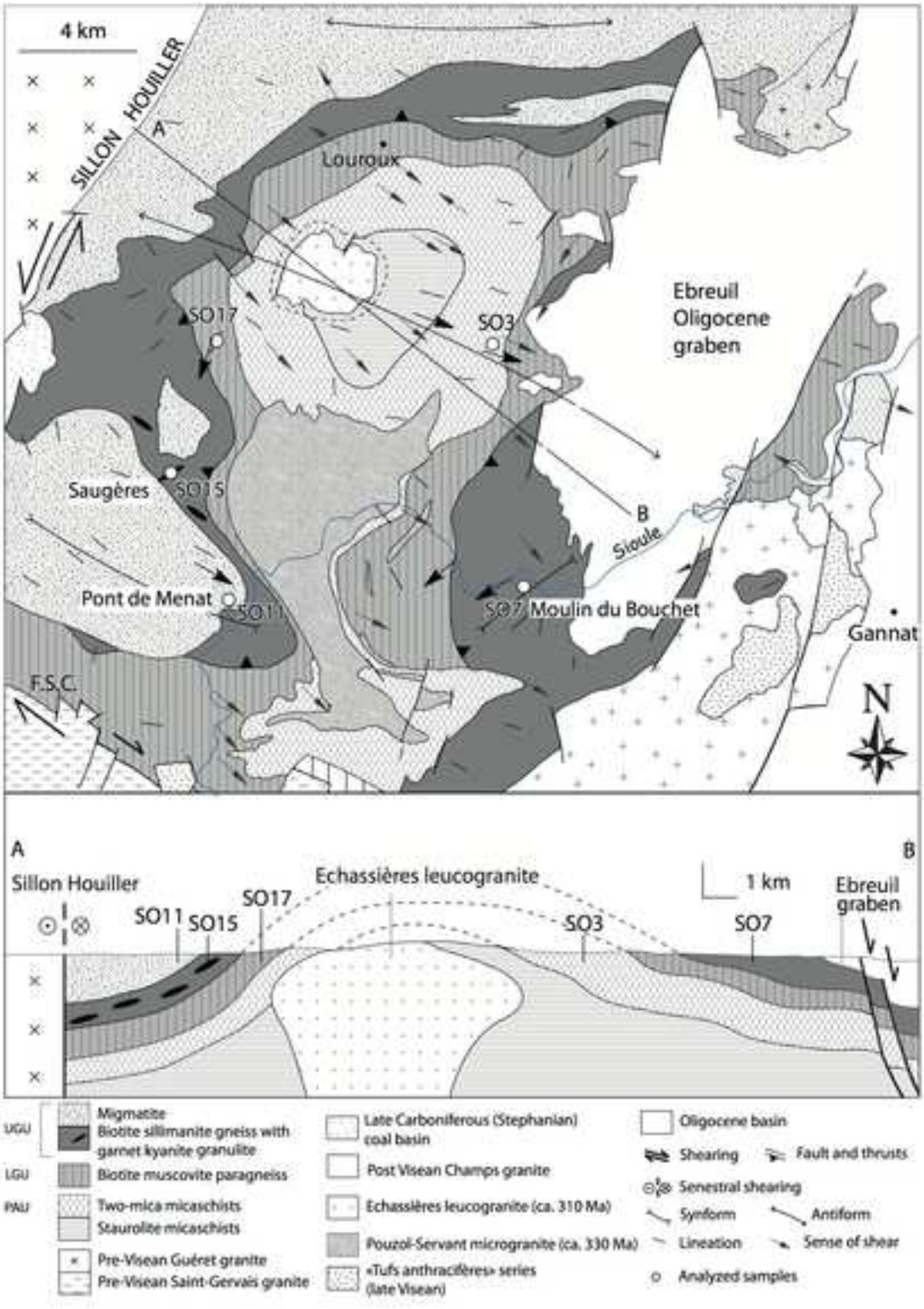

Fig. 2

Figure 3
Click here to download high resolution image

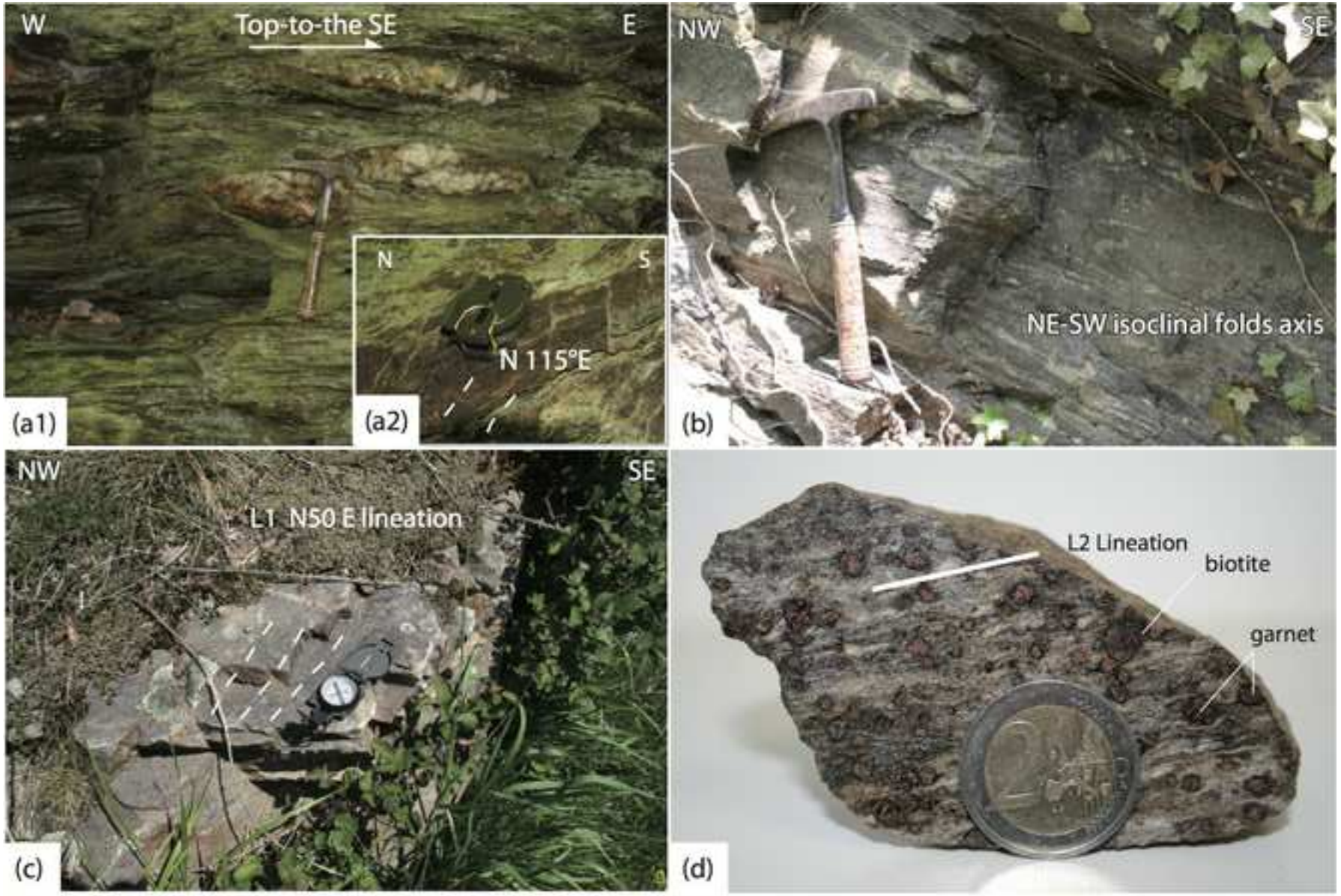

Fig. 3

Figure 4
Click here to download high resolution image

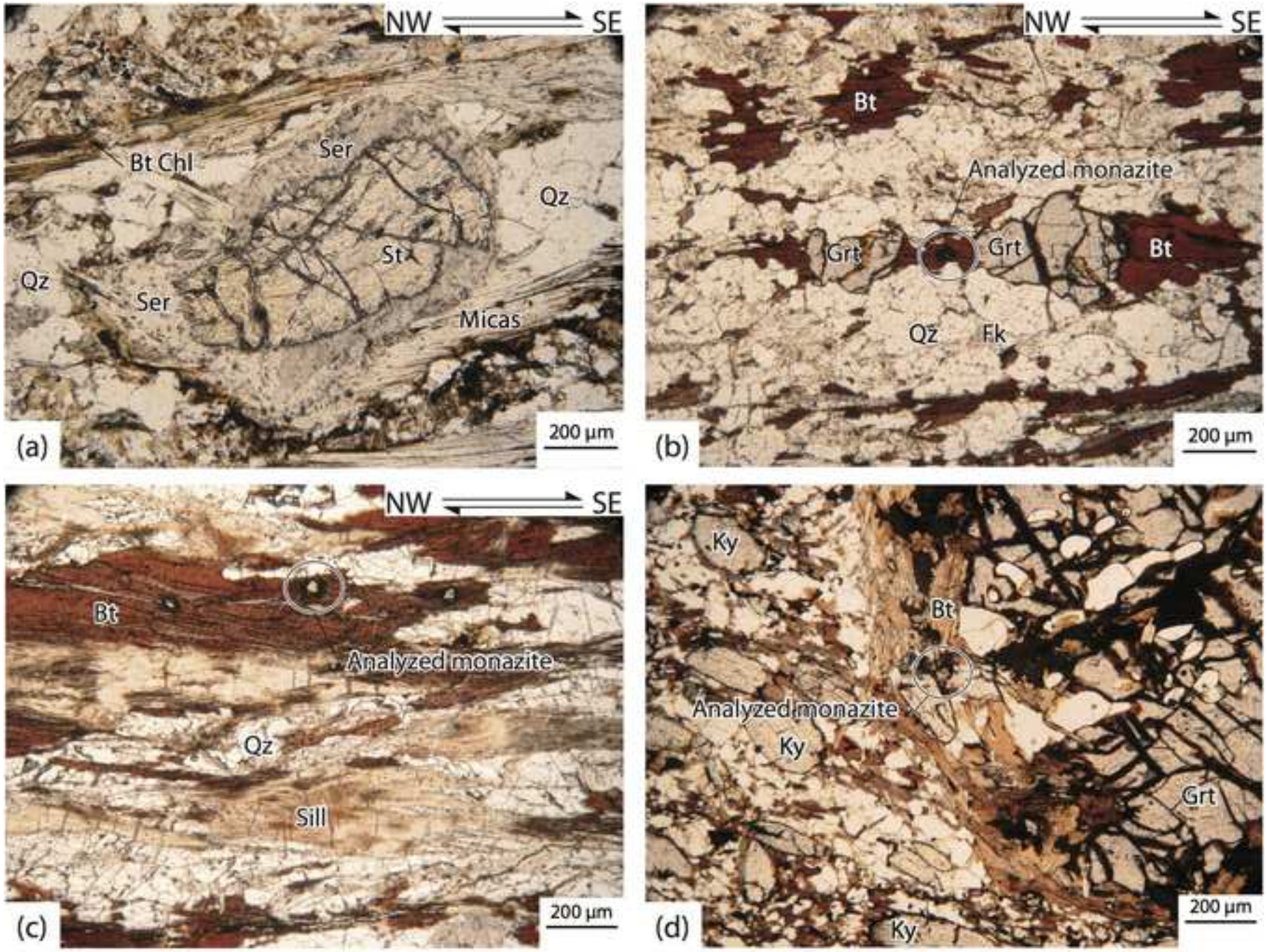

Fig 4

Figure 5
Click here to download high resolution image

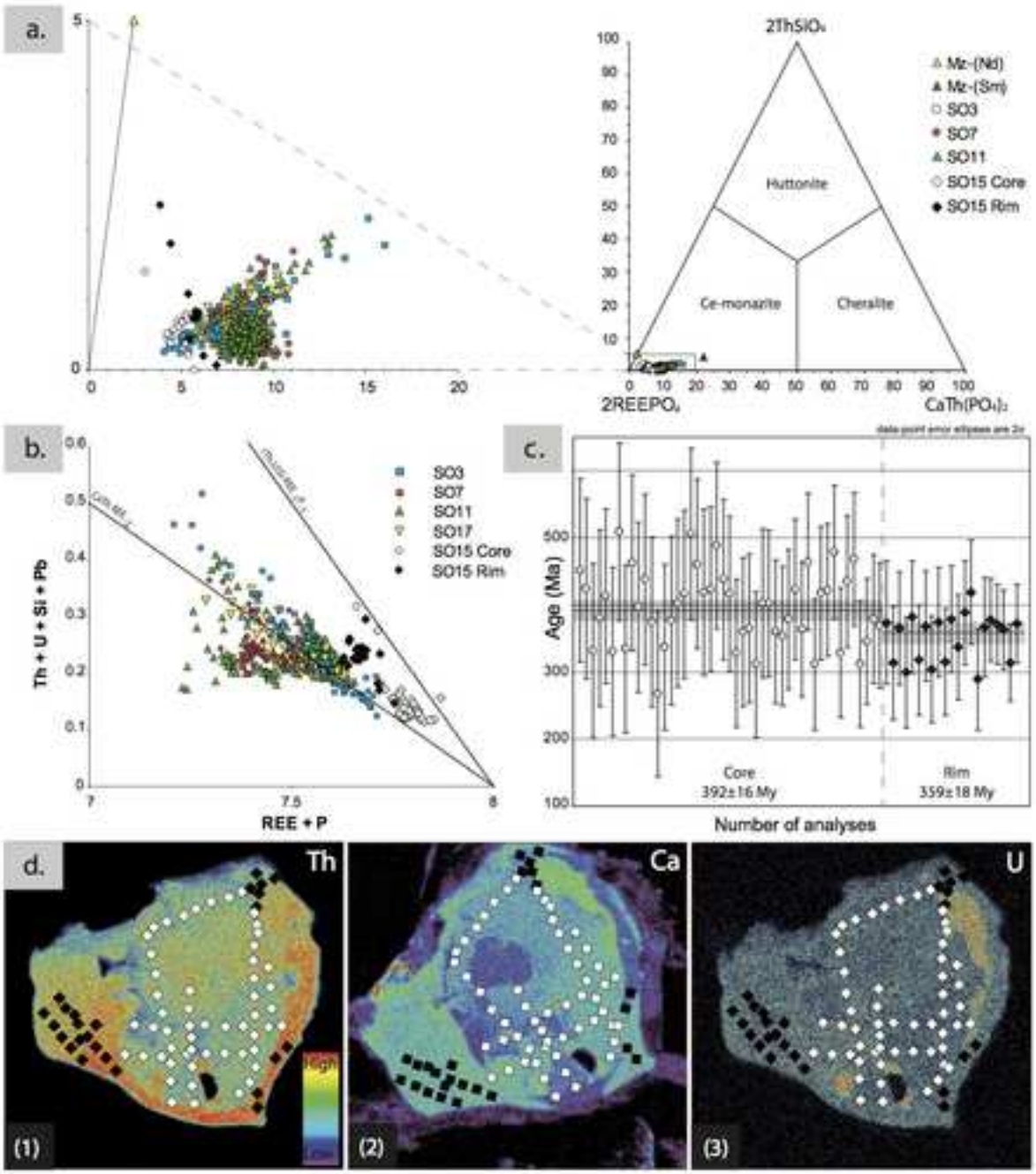

Fig. 5

Figure 6
Click here to download high resolution image

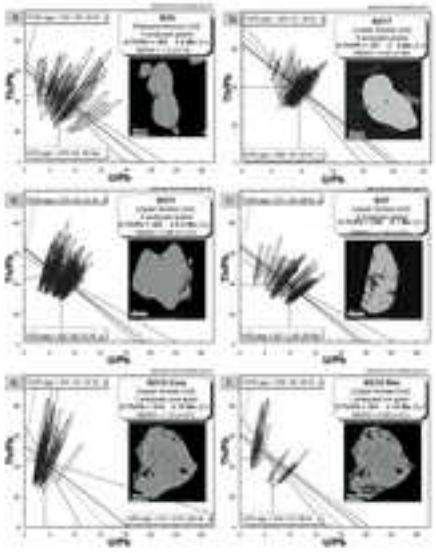

Figure 7
Click here to download high resolution image

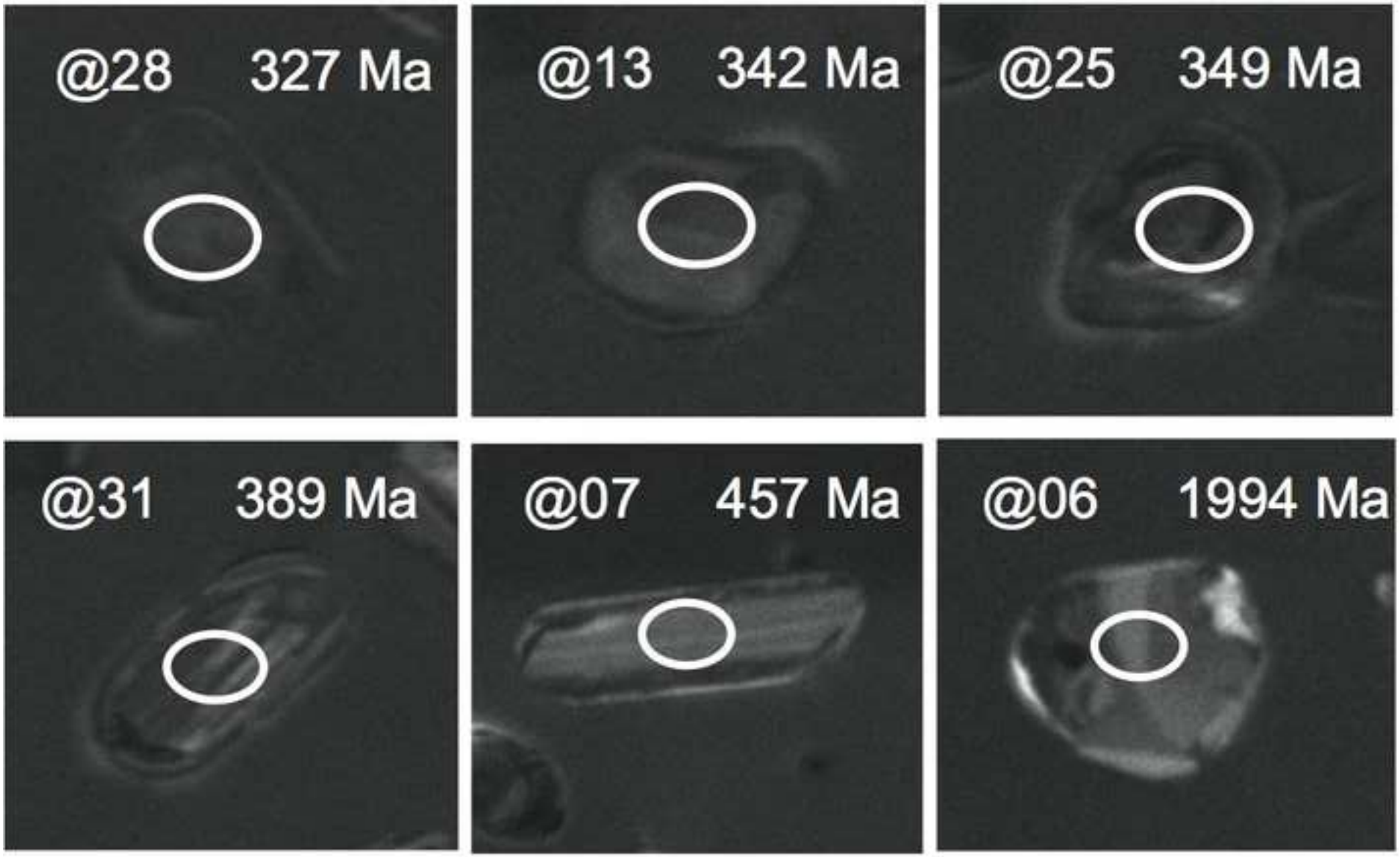

Fig. 2

Figure 8
Click here to download high resolution image

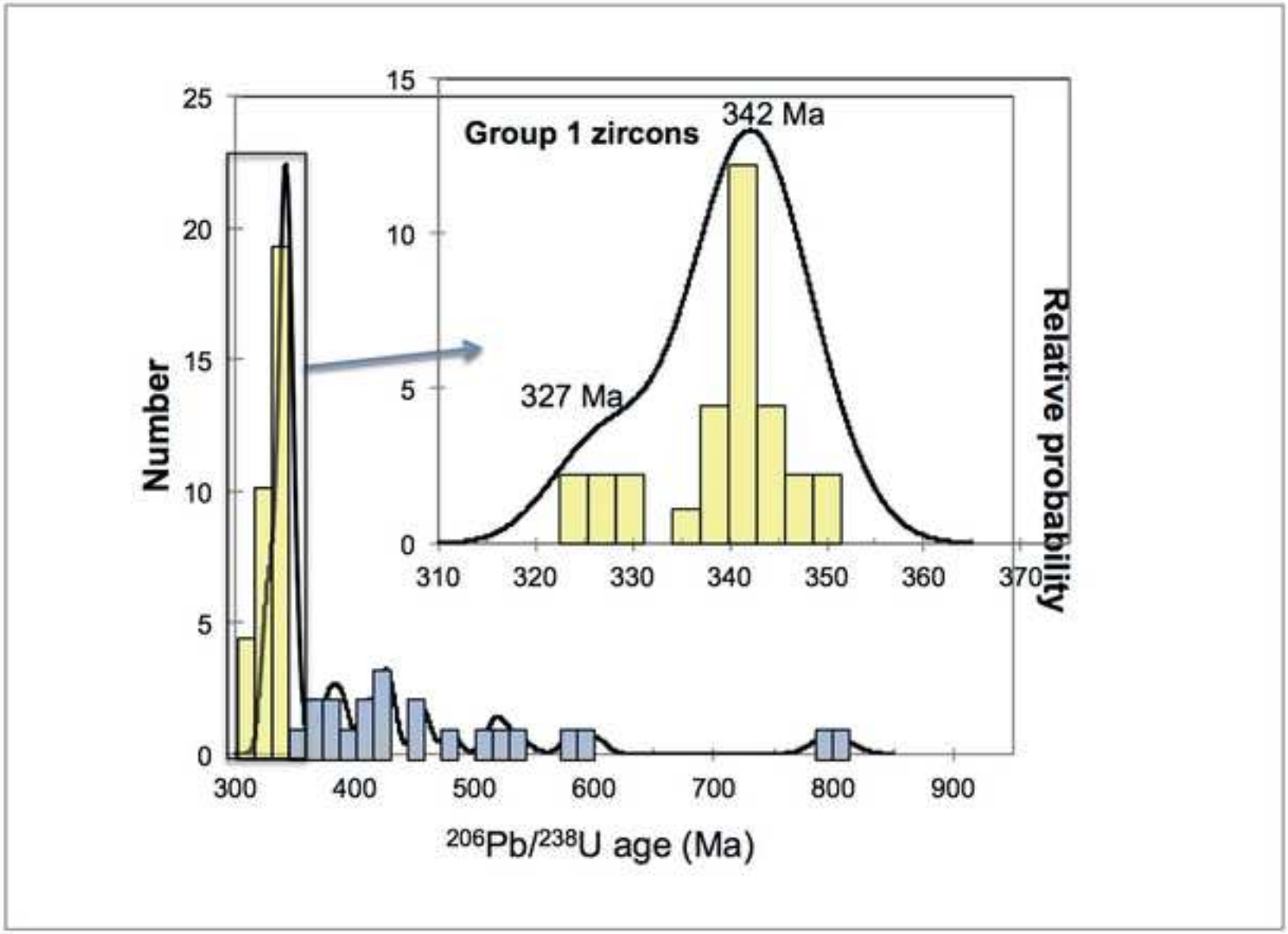

Figure 9
Click here to download high resolution image

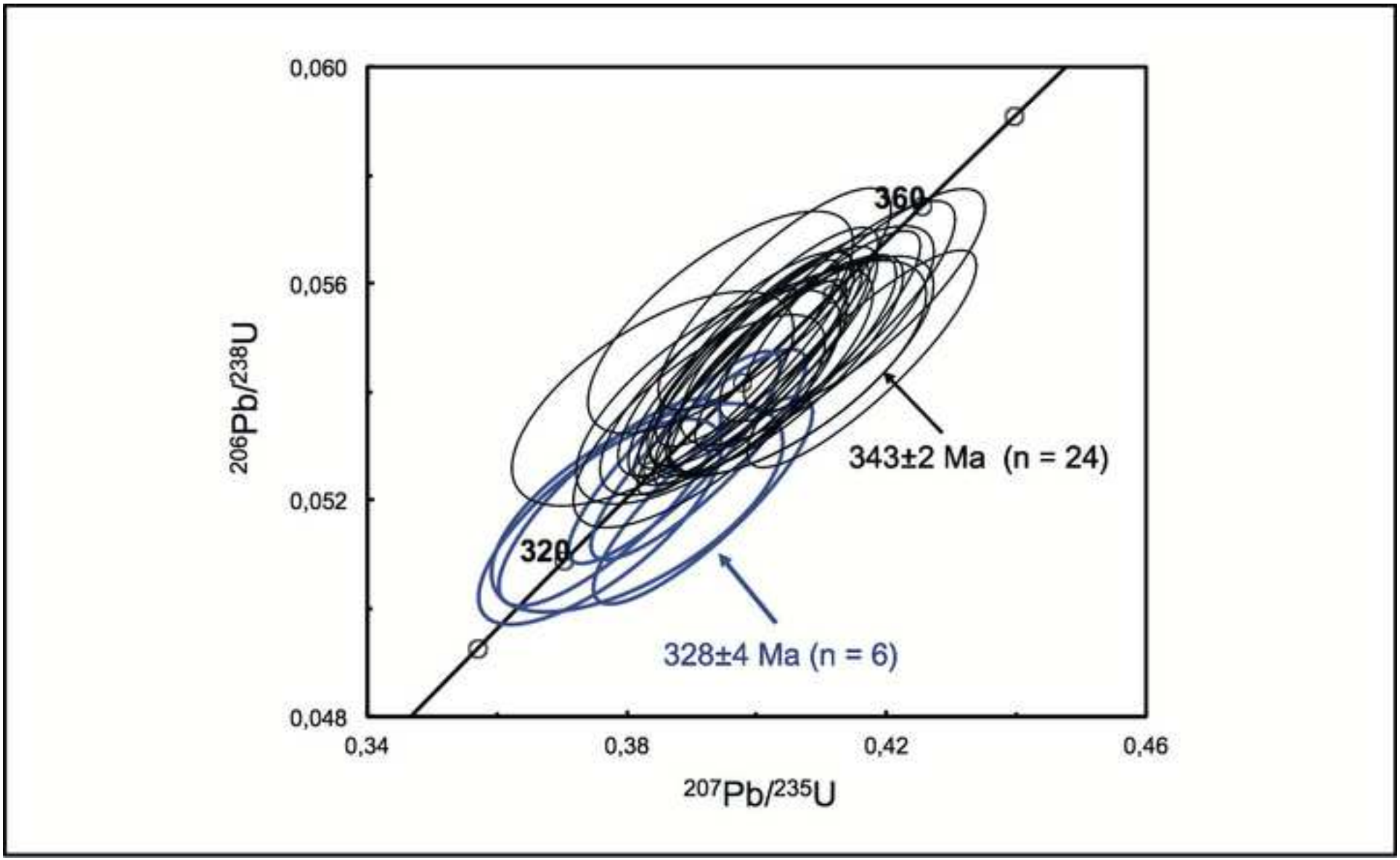

Figure 10
Click here to download high resolution image

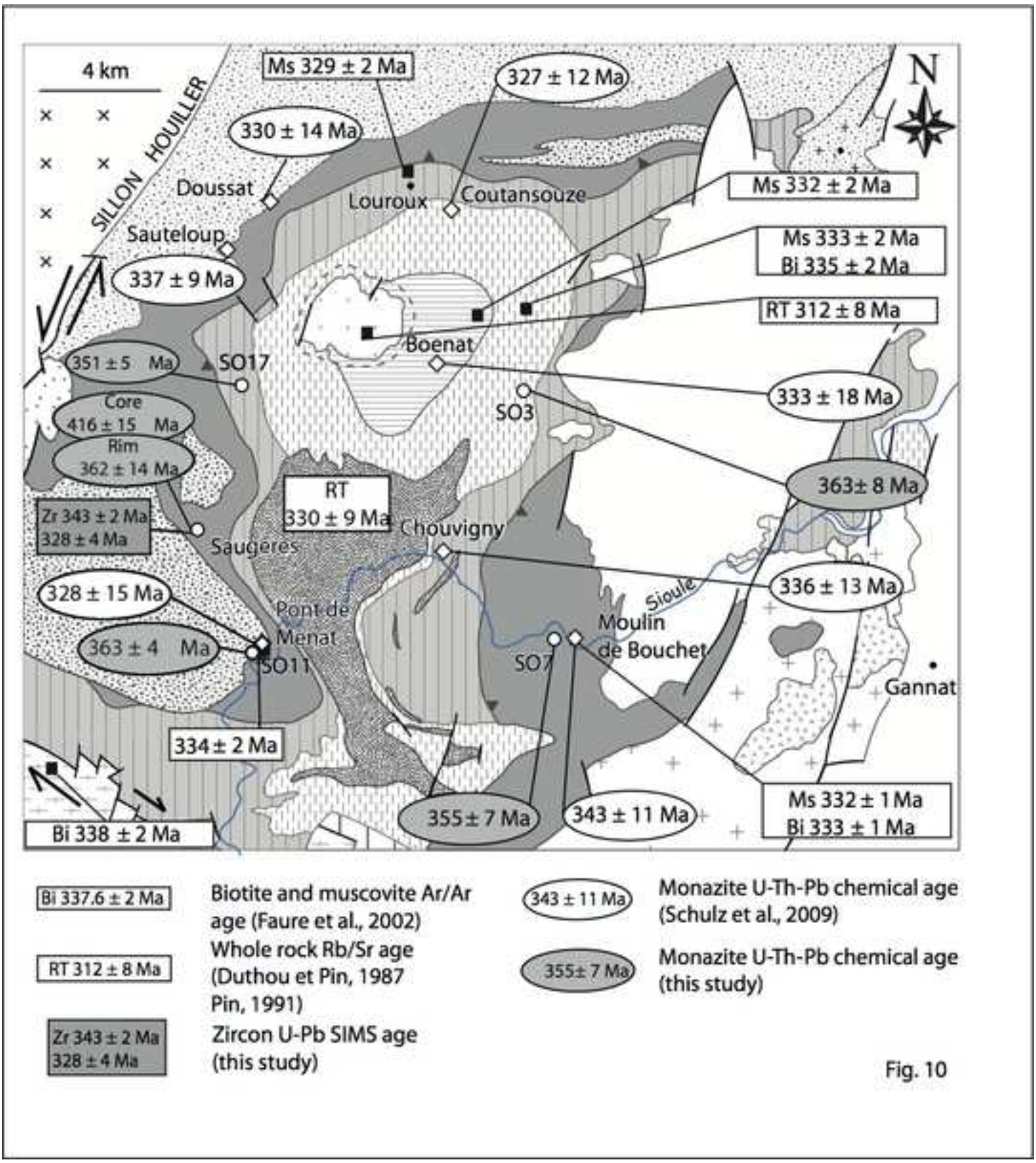

Fig. 10

Figure 11
Click here to download high resolution image

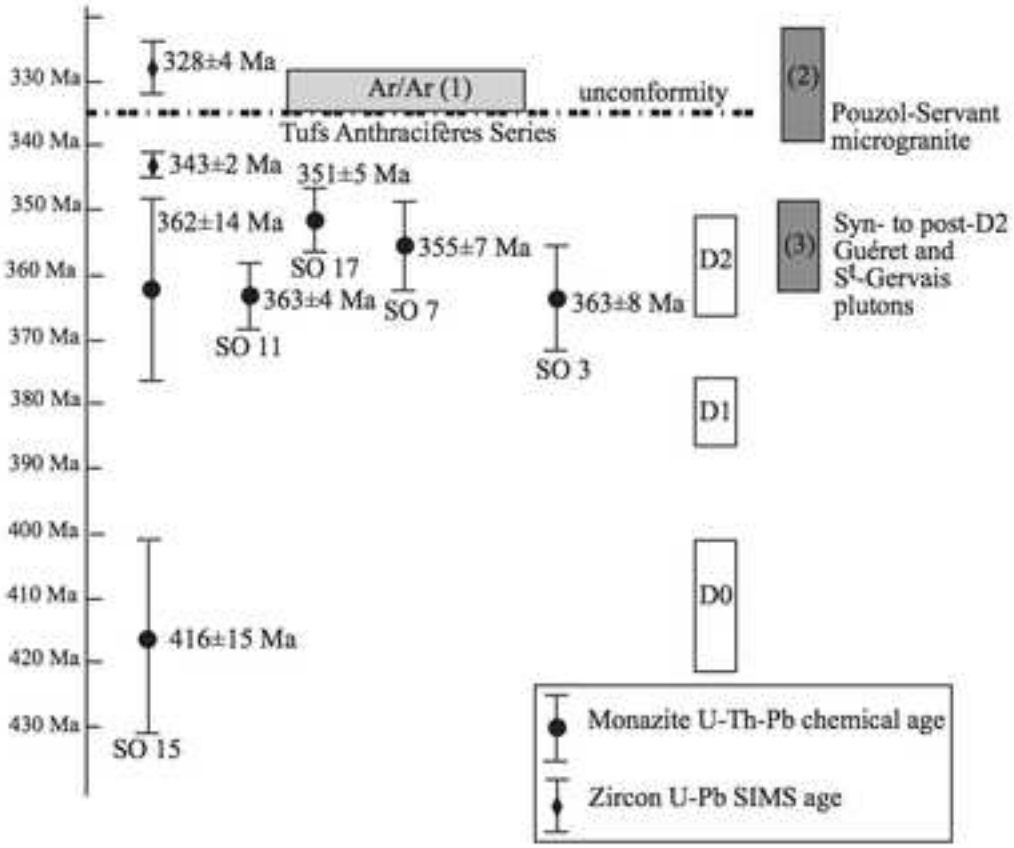

Fig. 11

Figure 12
Click here to download high resolution image

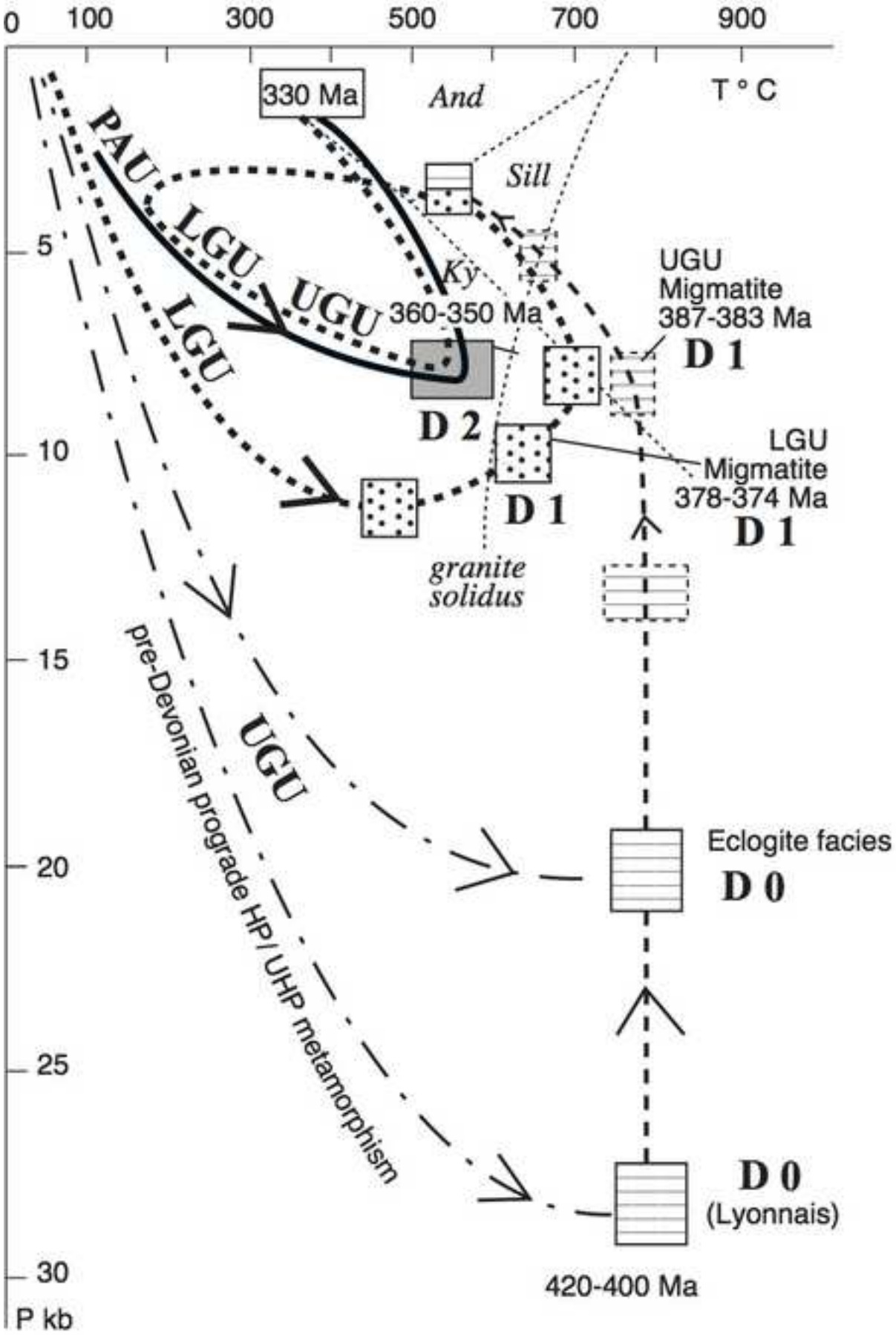

Fig. 12

Table 1. Dated sample locations and analytical data

Sample	LAT	LON	Nbr of grains	Pb (ppm)	U (ppm)	Th (ppm)	U/Pb	Th/Pb	Isochron age ±2σ	n
SO3	46°10'19.25"	3°01'30.80"	4	839 ± 253	4885 ± 1596	37366 ± 14335	6.2 ± 2.3	44.2 ± 8	363 ± 8	73
SO7	46°06'09.60"	3°02'28.20"	4	1013 ± 147	8039 ± 2514	39089 ± 5186	7.9 ± 2	39.1 ± 6.3	355 ± 7	73
SO11	46°06'01.19"	2°55'15.60"	4	914 ± 138	5365 ± 1296	39639 ± 5835	5.9 ± 1.2	43.8 ± 5.4	363 ± 4	174
SO15 Rim	46°07'46.99"	2°54'05.36"	1	586 ± 103	1960 ± 614	26843 ± 3470	3.4 ± 1	46.8 ± 7.9	361 ± 14	47
SO15 Core			1	808 ± 160	3922 ± 2648	38519 ± 3886	4.5 ± 2.2	49.5 ± 11.1	416 ± 15	21
SO17	46°10'31.26"	2°54'48.07"	6	1179 ± 235	8347 ± 1141	49787 ± 15110	7.2 ± 1.2	41.8 ± 4.8	351 ± 5	38

Table 2. Electron microprobe analyses of dated monazites

Sample	UO_2	PbO	Nd_2O_3	CaO	P_2O_5	ThO_2	Gd_2O_3	Ce_2O_3	SiO_2	Sm_2O_3	La_2O_3	Y_2O_3	Pr_2O_3
SO3	0.55 ± 0.18	0.10 ± 0.03	12.27 ± 0.54	0.88 ± 0.27	29.27 ± 0.5	4.25 ± 1.63	1.34 ± 0.28	29.27 ± 0.94	0.67 ± 0.99	2.21 ± 0.16	14.08 ± 0.78	0.99 ± 0.26	3.51 ± 0.15
SO7	0.91 ± 0.29	0.13 ± 0.02	11.16 ± 0.45	1.04 ± 0.11	28.82 ± 0.58	4.45 ± 0.59	1.57 ± 0.15	28.33 ± 0.51	0.28 ± 0.13	1.98 ± 0.16	13.9 ± 0.31	2.11 ± 0.64	3.29 ± 0.1
SO11	0.61 ± 0.15	0.1 ± 0.01	11.9 ± 0.32	0.99 ± 0.11	29.39 ± 0.92	4.48 ± 0.68	1.32 ± 0.29	28.85 ± 0.94	0.25 ± 0.11	2.03 ± 0.14	14.92 ± 0.6	0.74 ± 0.86	3.44 ± 0.11
SO15 Rim	0.22 ± 0.07	0.06 ± 0.01	12.34 ± 0.34	0.65 ± 0.49	29.33 ± 0.49	3.05 ± 0.39	0.51 ± 0.08	32.19 ± 0.37	0.15 ± 0.17	1.62 ± 0.12	16.55 ± 0.52	0	3.65 ± 0.09
SO15 Core	0.44 ± 0.3	0.09 ± 0.02	12.44 ± 0.23	0.81 ± 0.14	29.1 ± 0.48	4.39 ± 0.44	0.76 ± 0.14	30.78 ± 0.59	0.32 ± 0.15	1.93 ± 0.15	15.86 ± 0.32	0	3.57 ± 0.08
SO17	0.95 ± 0.13	0.15 ± 0.03	10.98 ± 0.55	1.35 ± 0.24	28.04 ± 1.03	5.67 ± 1.72	1.55 ± 0.13	27.26 ± 0.74	1.11 ± 2.79	1.88 ± 0.17	13.36 ± 0.39	2.56 ± 0.28	3.23 ± 0.13

Table 3

Table 3 SIMS U-Pb zircon data					Radiogenic isotopic ratios						Age (Ma)					
Sample/ spot #	[U] ppm	[Th] ppm	Th/U	f_{206} %	$^{207}Pb/^{206}Pb$	±σ %	$^{207}Pb/^{235}U$	±σ %	$^{206}Pb/^{238}U$	±σ %	$^{207}Pb/^{206}Pb$	±σ	$^{207}Pb/^{235}U$	±σ	$^{206}Pb/^{238}U$	±σ
SO-15A@01	904	28	0,03	0,00	0,0534	0,77	0,401	1,69	0,0544	1,50	346,5	17,3	342,2	4,9	341,6	5,0
SO-15A@02	231	94	0,41	0,01	0,0580	1,33	0,675	2,05	0,0844	1,56	530,5	28,9	523,8	8,4	522,3	7,8
SO-15A@03	743	34	0,05	0,00	0,0538	0,87	0,408	1,74	0,0549	1,51	364,6	19,4	347,3	5,1	344,8	5,1
SO-15A@04	673	21	0,03	0,00	0,0528	1,06	0,397	1,88	0,0545	1,55	320,0	23,8	339,4	5,4	342,2	5,2
SO-15A@05	819	25	0,03	0,01	0,0529	0,89	0,402	1,74	0,0550	1,50	326,6	20,0	342,8	5,1	345,2	5,0
SO-15A@06	289	83	0,29	0,03	0,1226	1,44	3,497	3,62	0,2069	3,32	1994,2	25,4	1526,5	29,0	1212,2	36,8
SO-15A@07	250	106	0,43	0,39	0,0534	1,75	0,541	2,31	0,0734	1,51	346,5	39,1	438,8	8,3	456,6	6,6
SO-15A@08	632	85	0,13	0,02	0,0703	1,81	1,295	2,48	0,1335	1,70	937,8	36,6	843,5	14,3	808,1	12,9
SO-15A@09	377	159	0,42	0,10	0,0565	1,07	0,527	2,19	0,0677	1,91	470,5	23,6	430,0	7,7	422,4	7,8
SO-15A@10	953	22	0,02	0,07	0,0532	0,82	0,387	1,72	0,0528	1,51	338,0	18,5	332,4	4,9	331,6	4,9
SO-15A@11	843	107	0,13	0,02	0,0545	0,92	0,517	1,77	0,0687	1,50	393,2	20,6	423,0	6,1	428,5	6,2
SO-15A@12	661	37	0,06	0,02	0,0553	0,87	0,416	1,74	0,0546	1,50	423,5	19,3	353,3	5,2	342,7	5,0
SO-15A@13	444	15	0,03	0,00	0,0538	1,08	0,404	1,85	0,0545	1,50	361,7	24,2	344,7	5,4	342,2	5,0
SO-15A@14	817	115	0,14	0,00	0,0569	0,69	0,534	1,72	0,0681	1,57	487,0	15,2	434,7	6,1	424,9	6,5
SO-15A@15	389	324	0,83	0,01	0,0583	0,91	0,668	1,75	0,0831	1,50	542,5	19,7	519,7	7,2	514,5	7,4
SO-15A@16	1693	280	0,17	0,09	0,0561	0,55	0,531	1,64	0,0687	1,54	454,6	12,1	432,4	5,8	428,3	6,4
SO-15A@17	582	213	0,37	0,00	0,0591	1,05	0,707	2,33	0,0868	2,08	569,0	22,7	542,9	9,8	536,7	10,7
SO-15A@18	585	31	0,05	0,02	0,0532	0,94	0,401	1,78	0,0547	1,52	338,4	21,1	342,4	5,2	343,0	5,1
SO-15A@19	757	28	0,04	0,02	0,0539	0,99	0,412	1,80	0,0555	1,50	367,2	22,2	350,6	5,3	348,1	5,1
SO-15A@20	396	141	0,36	0,00	0,0570	0,93	0,607	1,78	0,0773	1,52	490,3	20,3	481,7	6,8	479,9	7,0
SO-15A@21	616	27	0,04	0,01	0,0546	0,92	0,392	1,76	0,0520	1,50	397,7	20,6	335,6	5,0	326,7	4,8
SO-15A@22	1050	42	0,04	0,02	0,0537	1,26	0,408	1,96	0,0550	1,50	359,8	28,2	347,3	5,8	345,4	5,1
SO-15A@23	758	36	0,05	0,03	0,0537	0,86	0,391	1,73	0,0528	1,50	357,3	19,4	335,1	5,0	331,9	4,9
SO-15A@24	536	837	1,56	0,05	0,0547	0,98	0,458	1,80	0,0607	1,51	400,2	21,8	382,9	5,7	380,1	5,6
SO-15A@25	954	203	0,21	0,18	0,0543	1,03	0,417	1,82	0,0557	1,50	381,5	23,0	353,6	5,5	349,4	5,1
SO-15A@26	734	325	0,44	0,23	0,1111	0,63	3,048	2,00	0,1989	1,89	1818,0	11,5	1419,8	15,4	1169,6	20,3
SO-15A@27	735	413	0,56	0,02	0,1087	0,71	3,219	1,69	0,2147	1,54	1778,2	12,8	1461,7	13,2	1253,9	17,5
SO-15A@28	845	27	0,03	0,09	0,0527	1,09	0,377	1,85	0,0520	1,50	315,0	24,5	325,1	5,2	326,5	4,8
SO-15A@29	586	447	0,76	0,05	0,0696	0,75	1,251	1,77	0,1304	1,60	916,0	15,3	823,9	10,0	790,2	11,9
SO-15A@30	910	365	0,40	0,09	0,0568	0,78	0,575	1,69	0,0733	1,50	485,2	17,1	461,0	6,3	456,2	6,6
SO-15A@31	693	187	0,27	0,56	0,0555	1,57	0,476	2,18	0,0622	1,50	430,5	34,7	395,2	7,2	389,2	5,7
SO-15A@32	434	162	0,37	0,24	0,0557	1,21	0,479	1,98	0,0623	1,56	441,3	26,7	397,2	6,5	389,7	5,9
SO-15A@33	388	67	0,17	0,00	0,0541	1,09	0,451	1,86	0,0605	1,51	374,0	24,4	378,1	5,9	378,8	5,5
SO-15A@34	396	73	0,18	0,04	0,0550	1,10	0,495	1,89	0,0653	1,54	410,6	24,3	408,3	6,4	407,9	6,1
SO-15A@35	958	29	0,03	0,02	0,0529	0,77	0,398	1,69	0,0546	1,50	324,9	17,4	340,4	4,9	342,6	5,0
SO-15A@36	579	129	0,22	0,03	0,0540	0,93	0,437	1,78	0,0587	1,52	370,1	20,7	368,1	5,5	367,8	5,5
SO-15A@37	244	60	0,25	0,11	0,1003	2,17	1,531	2,84	0,1107	1,83	1629,2	39,8	942,8	17,6	676,9	11,8
SO-15A@39	1787	32	0,02	0,00	0,0529	0,61	0,397	1,63	0,0544	1,51	324,0	13,9	339,4	4,7	341,6	5,0
SO-15A@40	1767	22	0,01	0,05	0,0534	0,62	0,400	1,64	0,0543	1,52	347,3	14,0	341,8	4,8	340,9	5,0
SO-15A@41	1067	79	0,07	0,01	0,0533	0,70	0,398	1,66	0,0541	1,50	343,2	15,8	340,0	4,8	339,5	5,0
SO-15A@42	648	161	0,25	0,04	0,0541	1,14	0,491	1,97	0,0659	1,61	373,2	25,4	405,5	6,6	411,2	6,4
SO-15A@43	604	28	0,05	0,01	0,0538	0,92	0,404	1,77	0,0545	1,51	362,3	20,7	344,6	5,2	342,0	5,0
SO-15A@55	606	22	0,04	0,05	0,0541	1,39	0,407	2,05	0,0545	1,51	377,3	30,9	346,6	6,0	342,0	5,0
SO-15A@57	636	35	0,06	0,03	0,0531	1,36	0,391	2,03	0,0535	1,50	331,7	30,5	335,2	5,8	335,7	4,9
SO-15A@58	649	52	0,08	0,00	0,0608	0,94	0,818	1,84	0,0976	1,58	631,1	20,2	606,9	8,5	600,4	9,1
SO-15A@59	1977	1432	0,72	0,06	0,0593	0,64	0,772	1,63	0,0944	1,50	576,8	13,9	580,7	7,2	581,7	8,3
SO-15A@60	781	22	0,03	0,07	0,0528	1,37	0,376	2,04	0,0516	1,50	321,6	30,9	324,0	5,7	324,3	4,8
SO-15A@61	477	31	0,07	0,00	0,0539	1,57	0,405	2,17	0,0544	1,50	368,0	34,9	345,0	6,4	341,6	5,0
SO-15A@62	725	25	0,03	0,00	0,0530	1,28	0,395	1,97	0,0541	1,50	327,4	28,8	338,0	5,7	339,5	5,0
SO-15A@63	810	31	0,04	0,02	0,0533	1,21	0,399	1,93	0,0543	1,50	343,0	27,2	341,0	5,6	340,7	5,0
SO-15A@64	696	28	0,04	0,09	0,0534	1,87	0,382	2,41	0,0519	1,52	344,5	41,7	328,2	6,8	325,9	4,8
SO-15A@65	573	26	0,05	0,00	0,0528	1,50	0,393	2,12	0,0539	1,50	320,8	33,7	336,2	6,1	338,5	4,9
SO-15A@66	2192	98	0,04	0,11	0,0524	1,03	0,403	1,82	0,0557	1,50	304,3	23,3	343,7	5,3	349,5	5,1
SO-15A@67	577	227	0,39	0,15	0,0517	1,76	0,384	2,31	0,0539	1,50	272,0	39,8	330,0	6,5	338,3	4,9
SO-15A@68	609	16	0,03	0,00	0,0517	1,48	0,394	2,12	0,0553	1,52	274,2	33,5	337,6	6,1	346,9	5,1
Qinghu@1	1552	930	0,60	0,04	0,0496	0,92	0,173	1,80	0,0253	1,55	176,0	21,2	162,3	2,7	161,3	2,5
Qinghu@2	1209	554	0,46	0,00	0,0491	1,00	0,170	1,80	0,0252	1,50	150,4	23,3	159,6	2,7	160,2	2,4
Qinghu@3	2014	557	0,28	0,01	0,0502	0,95	0,174	1,78	0,0251	1,50	204,0	22,0	162,8	2,7	159,9	2,4
Qinghu@4	945	409	0,43	0,00	0,0500	1,94	0,172	2,45	0,0249	1,50	195,2	44,5	160,9	3,7	158,6	2,4
Qinghu@5	633	227	0,36	0,00	0,0490	1,40	0,170	2,06	0,0251	1,51	146,2	32,5	159,0	3,0	159,9	2,4
Qinghu@6	1362	797	0,59	0,11	0,0499	1,21	0,174	1,93	0,0253	1,51	188,3	27,9	162,6	2,9	160,8	2,4
Qinghu@7	2559	1041	0,41	0,01	0,0491	0,70	0,174	1,66	0,0256	1,50	153,9	16,4	162,6	2,5	163,2	2,4
Qinghu@8	1301	551	0,42	0,00	0,0496	0,96	0,171	1,78	0,0250	1,50	175,2	22,4	160,5	2,7	159,5	2,4
Qinghu@9	703	300	0,43	0,07	0,0482	1,46	0,165	2,09	0,0249	1,50	107,3	34,1	155,4	3,0	158,6	2,4
Qinghu@10	980	440	0,45	0,10	0,0498	1,23	0,174	1,94	0,0253	1,50	184,4	28,3	162,7	2,9	161,2	2,4
Qinghu@11	980	440	0,45	0,10	0,0498	1,23	0,174	1,94	0,0253	1,50	184,4	28,3	162,7	2,9	161,2	2,4
Qinghu@12	1144	478	0,42	0,08	0,0480	1,30	0,169	1,99	0,0256	1,50	98,0	30,5	158,7	2,9	162,8	2,4